Spatial proteomics and iPSC modeling uncover mechanisms of axonal pathology in Alzheimer's disease

Yifei Cai [1,*], Jean Kanyo [2], Raushan Wilson [2], Mohammad Shahid Mansuri [2,3], Pablo Leal Cardozo [3], Derek Goshay [4], Zichen Tian [1], Amber Braker [4], Kim Trinh [1], TuKiet Lam [2], Kristen J. Brennand [3,5], Angus C. Nairn [2,3,6], Jaime Grutzendler [1,7,*,#]

1. Department of Neurology, Yale University, New Haven, CT 06511
2. Yale/NIDA Neuroproteomics Center, Yale University, New Haven, CT 06511
3. Department of Psychiatry, Yale University, New Haven, CT 06511
4. Yale College, Department of Neuroscience, Yale University, New Haven, CT 06520
5. Department of Genetics, Yale University, New Haven, CT 06520
6. Department of Pharmacology, Yale University, New Haven, CT 06520
7. Department of Neuroscience, Yale University, New Haven, CT 06511

[*] Correspondence: yifei.cai@yale.edu, jaime.grutzendler@yale.edu

[#] Lead contact

ABSTRACT

Amyloid deposits in Alzheimer's disease (AD) are surrounded by large numbers of plaque-associated axonal spheroids (PAAS). PAAS disrupt axonal electrical conduction and neuronal network function, and correlate with AD severity. However, the mechanisms that govern their formation remain unknown. To uncover the molecular architecture of PAAS, we applied proximity labeling proteomics of spheroids in human AD postmortem brains and mice. We then implemented a human iPSC-derived AD model recapitulating PAAS pathology for mechanistic studies. Using this strategy, we uncovered hundreds of previously unknown PAAS-enriched proteins and signaling pathways, including PI3K/AKT/mTOR. Phosphorylated mTOR was highly enriched in PAAS and strongly correlated with disease severity in humans. Importantly, pharmacological mTOR inhibition in iPSC-derived human neurons or AAV-mediated knockdown in mice, led to a marked reduction of PAAS pathology. Altogether, our study provides a novel platform to examine mechanisms of axonal pathology in neurodegeneration and to evaluate the therapeutic potential of novel targets.

KEYWORDS

Proximity labeling, spatial proteomics, amyloid plaque-associated axonal spheroid, Alzheimer's disease, axonal pathology, iPSC-derived human neurons, PI3K/AKT/mTOR signaling pathway, AD human postmortem brain, PAAS proteome.

INTRODUCTION

A major pathological hallmark in Alzheimer's disease (AD) is the formation of aggregated extracellular β-amyloid peptide deposits [1]. However, the precise mechanisms by which amyloid deposits trigger downstream neuronal changes and contribute to cognitive deficits remains unknown. While amyloid plaques have been shown to cause overall synapse loss [2] and dendritic spine reduction in their vicinity [3], a less understood, yet potentially critical pathological hallmark is the development of axonal spheroids around plaques. Specifically, hundreds of axons in the vicinity of individual amyloid plaques develop enlarged spheroid-like structures (traditionally termed dystrophic neurites) [4-9]. These plaque-associated axonal spheroids (PAAS) are correlated with AD severity [10], and are predicted to markedly interfere with electrical conduction [11, 12], thus potentially altering neuronal networks and ultimately cognitive function. PAAS have been shown to contain high amounts of endolysosomal related vesicles [13, 14], which may be the result of malfunction in axonal transport [15-18] as well as in autophagy [14, 19] and proteolysis [13, 15]. Ultimately, axonal transport abnormalities associated with PAAS may cause distal synaptic dysfunction and axonal degeneration [3, 20]. In addition, it has been proposed that PAAS may play a role in the propagation of tau pathology through neuronal networks [21]. Therefore, PAAS have the potential for causing significant disruption of neuronal connectivity and cognitive impairment [3, 11, 12, 20, 22].

Despite their pathological importance, PAAS have not been a major focus of mechanistic or therapeutic investigations. Uncovering the molecular and cellular mechanisms involved in the formation of PAAS is a critical goal for the rational design of therapeutic approaches aimed at ameliorating axonal pathology in AD. In this study, we implemented an array of techniques and experimental tools to achieve this goal, including: spatially resolved proximity labeling proteomics to uncover the proteome of PAAS in human AD postmortem brains and AD-model mice; an iPSC-derived human neuronal-glial coculture AD model that recapitulates PAAS pathology; and genetic and pharmacological molecular manipulations in iPSC-derived human neurons and in mice. Together, these tools provided an opportunity to probe potential mechanisms by which proteomic hits from proximity labeling are involved in PAAS formation and growth.

Using these strategies, we identified hundreds of proteins that are enriched in PAAS. Bioinformatics analysis revealed these proteins are involved in protein-protein interaction (PPI) networks, such as endocytosis, phagosome and proteosome; as well as signaling pathways, such as the mTOR, calcium and axonal guidance pathways. Among the signaling pathways that were identified to be enriched in PAAS, we focused on the PI3K/AKT/mTOR pathway for several reasons. The pathway was prominently highlighted by our bioinformatic analyses, it is known to mediate autophagy and lysosome biogenesis [23-25], and its modulation may alter AD-like pathology in mouse models [26-28]. Importantly, we found that phosphorylated mTOR-S2448 (p-mTOR-S2448) was highly enriched in PAAS in postmortem human brains of patients with severe AD, compared to milder cases where it was nearly absent, suggesting a role of mTOR in mediating PAAS pathology. Indeed, using the human iPSC-derived AD model, we demonstrated that pharmacological inhibition of mTOR signaling markedly reduced PAAS. A similar effect was observed in AD-model mice when the mTOR signal was inhibited genetically or pharmacologically *in vivo*, thus indicating the therapeutic potential of mTOR signaling inhibition in axonal pathology in AD. Taken together, this study provides a theoretical and experimental

framework for analyzing axonal pathology in AD and beyond. Moreover, this study indicates a potential new strategy to alleviate axonal spheroids, independently of amyloid removal.

RESULTS

Proximity labeling of plaque-associated axonal spheroid proteins in postmortem brain

Proximity labeling is a recently developed methodology for biotinylating proteins in a subcellular compartment by genetic expression of localized peroxidases or biotin ligases in live cells [29-32]. This allows subsequent identification of the subcellular proteome by using LC-MS/MS technology [33, 34]. A modification of this approach was recently introduced for localized protein biotinylation in fixed tissues, by means of horseradish peroxidase (HRP)-conjugated antibodies targeted to a subcellular compartment [35-38]. We optimized these methodologies to uncover the proteome of PAAS in both human AD postmortem brains and AD-model mice (**Figures 1A-D, S1A-F**). For this we took advantage of the finding that phospholipase D3 (PLD3), an endolysosomal protein, is highly accumulated within PAAS around amyloid plaques (**Figures 1B and S1C**) [39, 40], and is specifically expressed in neurons [39] but not in glial cells (**Figures 1B and S1C, G**) compared to other endolysosomal markers, such as Lamp1 (**Figure S1C**). Furthermore, while low levels of PLD3 are also present in neuronal cell bodies (**Figure S1D**), semiquantitative immunofluorescence showed that the majority of PLD3 comes from PAAS (**Figure S1H**). This allowed us to use PLD3 as a protein bait for proximity labeling proteomics of PAAS (**Figures 1C-F and S1D, F**). Parallel experiments were performed using a protein bait enriched in neuronal cell bodies (NeuN), demonstrating the subcellular specificity of this technique (**Figure S1E**). Proximity-labeling proteomics involved the sequential incubation of postmortem AD human or mouse brains with primary antibodies against PLD3 and secondary HRP-conjugated antibodies, followed by a peroxidation reaction in the presence of hydrogen peroxide and Biotin-XX-Tyramide (**Figure 1A**). This led to robust biotinylation of proteins contained within PAAS, as evidenced by streptavidin labeling, with very low background outside the boundaries of these axonal structures (**Figures 1C-F and S1C-F**). Biotinylated proteins were pulled-down from lysed tissues and detected by streptavidin-HRP western blot, demonstrating a wide range of proteins, including the protein baits PLD3 (**Figures 1G and S1K**) or NeuN (**Figures S1J and L**). Thus, our antibody-based proximity labeling pipeline in postmortem tissues enables robust tagging and isolation of subcellularly localized proteins for subsequent mass-spectrometry-based proteomic profiling of axonal spheroids.

Proteomic analysis of plaque-associated axonal spheroids

To reveal the PAAS proteome, human postmortem brains of patients with intermediate to high AD neuropathology were processed for proximity labeling biotinylation of proteins within axonal spheroids. Parallel experiments were done with 15-month-old AD-model mice (5XFAD) for comparative analysis (**Figures 2A, S1A-B and Table S1**). By comparing the proteome derived from PLD3 antibody-labeled versus unlabeled AD brains, a total of 3,026 proteins were initially detected in AD humans and 2,371 proteins in 5XFAD mice (**Figures 2B, S2A-B and Table S3**). We applied a cutoff defined as p value < 0.05, false discovery rate (FDR) < 0.1 and fold change > 1 to differentiate true and false positives (**Figure 2B**). After applying these cut-off parameters, 368 and 917 proteins from AD humans and 5XFAD mice remained, respectively (**Figures 2B, S2C-D and Table S3**), among which 186 were shared between humans and mice (**Figure 2C**). Importantly, we were able to detect most of the proteins that had been previously identified to be enriched in PAAS (**Figures 2D-E, 3A, C, E, S3-1A and Table S2-3**)[5, 16, 18, 20, 41, 42].

Bioinformatic analysis using Gene Ontology (GO) annotation revealed that PAAS proteomic hits in humans and mice were classified within similar biological processes (i.e vesicle organization and fusion) and cellular components (i.e. presynapse, secretory vesicle) (**Figures 2F-G and Table S3**). These results reflected the axonal origin of PAAS and the massive accumulation of endolysosomal organelles within them. On the other hand, GO analysis of proteins that were excluded by the cutoff, showed a completely different classification pattern (**Figure S2E**). Moreover, proximity labeling of proteins in a different neuronal subcellular compartment using the protein bait NeuN as a bait, yielded a completely different proteome (**Figure S2F and Table S3**), highlighting the subcellular specificity of our proximity labeling proteomics pipeline.

Uncovering the molecular architecture of plaque-associated axonal spheroids

To further understand the protein networks and signaling involved in axonal spheroid pathology, we next performed protein-protein interaction analysis. We identified five main protein clusters in humans: endocytosis, phagosome, synapse, proteasome and ubiquitin-mediated proteolysis (**Figure 3A-B and Table S3**). These clusters comprised around ~50% of the PAAS proteome in humans and were mostly conserved in mice (**Figures S3-1A and B**). This is in agreement with the current cell biology knowledge, showing that the majority of the PAAS volume is occupied by endolysosomal vesicles [13, 14]. Notably, using signaling pathway analysis, we uncovered many pathways that were not previously appreciated to be involved in PAAS such as axon guidance, calcium and mTOR signaling (**Figures 3D, S3-1C-F and Table S3**), in addition to those related to the known PAAS cell biology (**Figure 3D, S3-1C, S3-1G-H and Table S3**). These results were cross-validated using gene set enrichment analysis (GSEA), which highlighted similar signaling pathways, including lysosome, proteosome, ubiquitin mediated-proteolysis and mTOR (**Figures S3-1I-J and Table S3**).

Guided by the proteomic analysis, we next selected a diverse set of proteomic hits for further validation by means of high-resolution immunofluorescence confocal imaging (**Figures 3E and S3-2**). We discovered proteins not previously known to be present in PAAS, that are involved in diverse cell biological functions (see diagram in **Figures 3E, S3-2 and Table S2**). Amongst those, we found lysosome-related proteins GAA, GBA and TPP1 (**Figures 3E, S3-2A-B and S3-2P-Q**); phagosome protein ATP6V0A1 (**Figures 3E and S3-2C**); fusion and endocytosis-related protein SYT11 (**Figures 3E and S3-2D**); actin cytoskeleton proteins RAC1 and SPTBN1 (**Figures 3E and S3-2E-F**); stress granule markers G3BP1 and G3BP2 (**Figures 3E and S3-2L-O**); calcium signaling molecules CAMK2A, ATP2B3, CACNA2D1 and CACNA1B (**Figures 3E, S3-2G-K and R**); PI3K/AKT/mTOR pathway-related proteins PIK3R4, AKT1, mTOR, LAMTOR, RAGA, RAGC and RAPTOR (**Figures 3E, 4A and S4A**), as well as transmembrane proteins and receptors ITM2B and NTRK2 (**Figures 3E and S3-2M-N**). Comparative analysis of protein abundance and subcellular distribution revealed similarities and differences between mice and humans (**Figures S3-2A-B v.s. P-Q; G v.s. R; and S4B**) that are likely to be important for future data interpretation. Altogether, our data revealed previously unappreciated protein networks and signaling pathways that may be critical for the pathogenesis of PAAS.

Phosphorylated mTOR accumulates within axon spheroids as Alzheimer disease progresses

Our data directed our attention to the mTOR signaling pathway, given that it is one of the most significant pathways in our proteomic analysis (**Figures 3D-E and S3-1C, D, J**) and that it plays critical roles in autophagy, lysosome biogenesis and local protein synthesis [23-25].

Immunofluorescence staining showed that proteins involved in mTOR signaling are enriched in axonal spheroids in postmortem human brains of patients with both mild cognitive impairment (MCI) or AD (**Figures 4 and S4A-B**). Strikingly, phosphorylated-mTOR-S2448 was highly enriched in spheroids of patients with intermediate to high AD neuropathology but not in those with low AD neuropathology (**Figures 4B-C**), indicating that this protein can be used as a hallmark to distinguish AD brains at various disease stages (**Figure 4D**). Furthermore, this raises the possibility that the mTOR signaling pathway may be mechanistically involved in the formation and growth of axonal spheroids around plaques.

Human iPSC modeling recapitulates PAAS pathology

To establish a broad strategy to genetically and pharmacologically manipulate selected proteomic hits to investigate their potential roles in spheroid formation, we made use of long-term human iPSC-derived *NGN2*-induced glutamatergic neuron [43] and astrocyte co-cultures (**Figures 5A-B and S5A-B**). This system has recently been shown to be capable of recapitulating the formation of axonal spheroids following administration of exogenous aggregated beta amyloid [44]. Our optimized model showed the formation of ThioflavinS positive amyloid deposits (**Figures 5B and S5C**) that were surrounded by massive halos of axonal spheroids. These spheroids were enriched with autophagosomes and lysosomes (**Figures 5B-C and S5D, F**), and expressed phosphorylated Tau S235, S396 and S404 (**Figure S5E**), thus greatly resembling axonal spheroids in humans (**Figure 1B**). This human iPSC-derived AD model is a versatile system that allows efficient pharmacological and viral-mediated manipulations, thereby allowing mechanistic investigation of PAAS pathology in human neurons.

mTOR signaling inhibition reduces PAAS pathology in human neurons

We next tested the role of PI3K/AKT/mTOR signaling in the formation and growth of axonal spheroids. Like in postmortem human brain (**Figures 4A and S4A**), our iPSC-derived AD model demonstrated similar enrichment of proteins involved in the PI3K/AKT/mTOR signaling pathway (**Figures 5C and S5F**). We thus tested whether pharmacological inhibition of mTOR, using Torin1, an mTORC1 and mTORC2 inhibitor [45, 46], had any impact in the overall degree of axonal spheroid pathology. Our results showed that Torin1 treatment was able to reduce p-mTOR S2448 expression in PAAS (**Figures 5D-E**), indicating target engagement. Importantly, we found that both the size of individual spheroids as well as the overall number of spheroids was markedly reduced following this treatment (**Figures 5F-I**), without significant changes in axonal density (**Figure 5J**), neuronal soma or amyloid plaque size (**Figures 5K, S5G and S5H**). These data suggests that mTOR signaling is involved in the progression of amyloid-induced axonal spheroid formation in human neurons.

mTOR signaling inhibition reduced PAAS pathology *in vivo*

To determine if the effect of mTOR signaling inhibition is conserved in the *in vivo* setting, we developed a method for viral-mediated genetic knockdown of proteins in neurons in the mouse brain, using a Cre/lox system (**Figures 6A-C and S6A-B**). To achieve this, we used heterozygous *Mtor*-floxed-5XFAD mice [47], and infected them with AAV9-hsyn-cre-2a-tdTomato virus, which allows sparse neuronal infection and visualization of individual spheroids (**Figures 6D-E**). Analysis of this treatment showed that individual axonal spheroid sizes were reduced by mTOR knockdown (**Figure 6F-G**). To determine if the overall spheroid halo sizes were also affected by this treatment, we next infected mice with AAV-PHP.eB-CAG-GFP vector which allows efficient

neuronal infection (**Figures 6H and S6C**). Our results showed that in addition to individual axonal spheroids around plaques, heterozygous *Mtor* knockout significantly reduced the size of the overall axonal spheroid halos around plaques (**Figure 6I-J and S6D**). Importantly, these treatments had no effect on either amyloid plaque size (**Figure S6F**) nor overall neuronal cell body size (**Figures 6K and S6E**), which could potentially confound interpretation of the observed reduced spheroid pathology. Our *in vivo* results in mice were consistent with our *in vitro* results using human neurons, and indicate that mTOR signaling may be a potential therapeutic target for reducing axonal spheroid pathology.

DISCUSSION

Despite the fact that dystrophic neurites around plaques were identified more than a century ago [9] and they are one of the most prevalent neuropathological hallmarks in AD [10, 13, 48, 49], these plaque associated axonal spheroids have not been systematically studied because of a lack of appropriate methodologies [4, 6]. In this study, we implemented for the first time a comprehensive approach including spatial proteomics, human iPSC-derived neuronal modeling and *in vivo* mouse genetic manipulations, to investigate the molecular and cellular mechanisms of PAAS formation. Specifically, we optimized proximity labeling proteomics methodologies based on antibody-mediated biotinylation [35], which allowed us to uncover the molecular architecture of PAAS in postmortem human brains and AD-model mice. Using bioinformatics analysis and high-resolution confocal imaging validation, we identified many proteins and signaling pathways previously not known to be enriched in PAAS. To investigate the functional implications of these pathways on the pathogenesis of axonal spheroids in humans, we optimized a human iPSC-derived neuron-astrocyte co-culture system [44] that recapitulates the formation of PAAS. Axonal spheroids in this model strikingly resemble those seen in humans, including their massive accumulation of endolysosomal vesicles [13, 14] and cytoskeletal features, such as tau hyperphosphorylation [21, 50]. Collectively, our subcellularly resolved axonal spheroid proteomic database combined with a tractable iPSC axonal spheroid modeling, and *in vivo* genetic manipulations constitutes an important approach for future mechanistic investigation and therapeutic testing aimed at axonal spheroid pathology in AD. Specifically, our studies indicate the therapeutic potential of mTOR signaling for reducing axonal spheroid pathology.

Uncovering the axonal spheroid proteome using proximity-labeling proteomics

Proximity labeling proteomics with subcellular resolution is a technique that overcomes the lack of cellular and subcellular specificity of conventional tissue proteomics of micro-dissected amyloid plaques [51-53]. Importantly, the use of an antibody-based biotinylation approach [35, 36] to tag proteins in axonal spheroids, without the need for overexpression of an exogenous peroxidase or biotin ligase [29, 30, 33], allowed us to obtain a comparative proteome in humans and mice, using widely available postmortem tissues. We used PLD3 as an antibody bait because this lysosomal protein is highly enriched in PAAS of both humans and mice [39, 40]. Furthermore, PLD3 is almost exclusively expressed in neurons [39], thus reducing the potential for lysosomal contamination from other cell types.

Using this proteomic strategy, we identified many proteins that were unknown to be enriched in PAAS as well as those previously identified in these structures (**Table S2 and S3**), Many of the PAAS-enriched proteins were presented in both humans and mice, suggesting conserved mechanisms in the formation of spheroids. Bioinformatic analysis highlighted five main conserved networks of protein-protein-interactions including endocytosis, synapse, phagosome, proteosome and ubiquitin-mediated proteolysis (**Figures 3A-C and S3-1A-B**). In addition, it also revealed signaling pathways including axon guidance, actin cytoskeleton, calcium, mTOR signaling and others (**Figures 3D and S3-1C-F, J**). We also noticed differences in expression levels and subcellular protein distributions between species, such as in GBA, SYT11, CAMK2, TPP1 and mTOR (**Figures S3-2A, D, G, P-R and S4B**). This suggests possible distinct molecular and cellular mechanisms and highlights the importance of performing parallel molecular studies in mice and humans.

Among the diverse signaling pathways identified by proteomics analysis, several possible mechanisms may be involved in PAAS formation and growth, including cytoskeletal deregulation, proteolysis dysfunction, calcium homeostasis, and mTOR signaling. In terms of cytoskeletal deregulation, we found that PAAS were enriched in various proteins belonging to signaling pathways such as axon guidance (**Figures 3D and S3-1F**), actin cytoskeletal signaling (**Figure S3-1C**), dynein heavy chain binding, filamin binding and Ral GTPase binding (**Figure S3-1A-B**). This suggests that cytoskeletal reorganization and plasticity could be important events in the initial formation and enlargement of PAAS. One possibility is that such cytoskeletal changes could impact retrograde and anterograde axonal cargo transport, ultimately leading to accumulation of endolysosomal vesicles [16, 54, 55] and the consequent expansion of the axon into a spheroid. Regarding proteolysis dysfunction: proteomics data revealed accumulation of proteins involved in endocytosis, phagosome, proteosome, ubiquitin-mediated proteolysis and lysosome acidification (ATPase complex) (**Figures 3A, B, D and S3-1A-C**). Previous data showed protease-deficient lysosomes and autophagosome accumulated within PAAS [13], while disruption of lysosomal proteolysis caused axonal dystrophy [15]. The data suggests that focal disruption in lysosomal function within axonal segments around plaques can cause spheroid formation and growth. Pertaining to calcium homeostasis, we showed that calcium signaling proteins, such as CAMK2, calmodulin and voltage-gated calcium channel proteins CACNA1B and CACNA1D1 (**Figures 3D-E, S3-1E and S3-2G-K, R**), are enriched in PAAS suggesting that local calcium signaling dysregulation plays a role in PAAS pathogenesis. Interestingly, recent data showed abnormal local calcium efflux from deacidified late endosomes and amphisomes affecting axonal transport of these vesicles in PSEN1 knockout mice [56]. As for mTOR signaling, the PI3K/AkT/mTOR pathway was prominently highlighted in several of our bioinformatic analyses (**Figures 3D-E, S3-1D, E, J**). Importantly, we found that in human postmortem brain, phosphorylated mTOR is highly enriched in axonal spheroids (**Figures 4A-B and S4A, D**), and its levels correlated with the severity of disease (**Figures 4B-D**). Given that PI3K/AKT/MTOR signaling can inhibit cell autophagy and lysosomal biogenesis, an intriguing possibility is that dysregulated mTOR signaling could be an early mechanism in the accumulation and dysfunction of endolysosomal organelles [11, 12] leading to spheroid expansion.

iPSC modeling and genetic *in vivo* molecular modulation uncover targets with therapeutic potential

In recent years, human iPSC technology has facilitated investigation of Alzheimer mechanisms [57-61]. To further understand the mechanistic role of signaling molecules found to be enriched in PAAS, we optimized a human iPSC neuron-astrocyte co-culture model [44] that recapitulated well the hallmarks of Alzheimer's disease, including amyloid deposits, axonal spheroids and intraneuronal hyperphosphorylated tau. This system allowed for the first-time testing of the role of selected pathways potentially involved in PAAS pathology using genetic and pharmacological manipulations in human neurons. Together with our *in vivo* viral vector-mediated manipulations in AD-model mice, these methods constitute a comprehensive approach to examine potential targets derived from our proteomic dataset.

As a proof of concept, we focused on PI3K/AKT/MTOR signaling given that it was one of the most highlighted pathways by multiple bioinformatic analyses of our PAAS proteomics data (**Figures 3D-E, S3-1D, E, J**) and phosphorylated mTOR was found to be a strong marker of severe

PAAS pathology (**Figures 4A-B and S4A, D**). Using the iPSC-derived AD model we showed that pharmacological inhibition of mTOR signaling led to a marked reduction in PAAS pathology (**Figures 5D-J**). Furthermore, viral vector-mediated genetic knockdown of mTOR in AD-model mice (**Figures 6A-B and S6A-E**), also demonstrated a reduction in PAAS (**Figures 6C-E and S6D-E**). While mTOR is known to be a regulator of cell growth and maturation [25, 45], our mTOR manipulations did not affect overall neuronal cell body size nor axon density (**Figures 5J, K and S5G**). Thus, the effect of mTOR modulation was selective to PAAS, supporting the role of the PI3K/AkT/mTOR singling pathway in PAAS formation or growth and highlighting its therapeutic potential.

Although the sequence of events leading to spheroid formation remains unclear, our data supports the idea that spheroids form as a result of extracellular amyloid deposition rather than themselves being the source of focal amyloid deposition [16, 62]. The causal effect of aggregated extracellular amyloid is clearly demonstrated in our human iPSC experiments, where we show that exogenous administration of amyloid can induce PAAS that resemble those in humans and mice. Even though in this model neurons are widely exposed to diffuse amyloid β, axonal spheroids were only observed in the vicinity of compact thioflavin S positive deposits (**Figures 5B, S5C and S5F**). This is consistent with previous observations in humans showing that many diffuse amyloid deposits (those labeled with anti-amyloid β antibodies but not with thioflavin S), are not surrounded by PAAS, while the vast majority of thioflavin S positive deposits have extensive PAAS around them [63].

Axonal spheroid pathology can also be found in other neurodegenerative disorders, such as Niemann-Pick disease type C [64], Nasu Hakola disease [65], leukoencephalopathy caused by CSF1R mutations [66], Huntington's disease [67] and others. Thus, the proteomic dataset, iPSC-derived AD model and *in vivo* mouse genetic manipulation strategies that we established will facilitate future mechanistic studies addressing the diversity of cell biological processes that govern axonal spheroid pathology in AD and other neurodegenerative disorders.

Limitations and future directions

There are several potential limitations of the current study. First, given the proximity labeling reaction radius is reported to be around 10-20 nm, some proteins that are not in close proximity to PLD3 may have not been detected in the PAAS proteome. However, PLD3 is highly enriched in axonal spheroids, thus increasing the probability of protein biotinylation. This is evidenced by the fact that we were able to capture the majority of proteins previously described to be enriched in axonal spheroids (**Figures 3 and S3-1**). Second, although PLD3 is enriched in spheroids of both AD humans and mice, some labeling occurs at neuronal cell bodies (~27% of PLD3 signal is derived from cell bodies) (**Figures S1D and S1H**) [68, 69]. Thus, our proteomics dataset may include some neuronal cell body-specific proteins, in addition to those specifically expressed in axonal spheroids as well as in both cellular compartments. Third, we were unable to compare the levels of the various PAAS proteins at different stages of disease progression because the reduced number of plaques and axonal spheroids in very early stages of the disease markedly limited the signal-to-noise ratio of the proteomic analysis. Alternatively, quantitative protein comparisons at different stages of disease could be done using emerging techniques for multiplexed high resolution quantitative imaging [70]. While we show that the human iPSC-derived AD model recapitulates the formation of spheroids around amyloid plaques, this occurs in a relatively rapid

manner that may not reflect the *in vivo* situation. Thus, future models may need to be perfected for more chronic buildup of amyloid deposits. In addition, co-culturing with other cell types, such as microglia, may provide additional features that better resemble the *in vivo* plaque microenvironment.

FIGURE LEGEND

Figure 1. Proximity labeling of proteins within plaque-associated axonal spheroids

A. A schematic shows the pipeline of proximity labeling PAAS proteomics in postmortem brains. **B.** Immunofluorescence confocal deconvolved image shows PLD3 is highly enriched in axonal spheroids (red, PLD3) around amyloid plaques (blue, ThioflavinS) in postmortem AD human brain. **C-F.** Proximity labeling biotinylation of proteins within PAAS in **(C)** human AD and **(D)** 5XFAD mouse brains. **(C-D)** Biotinylated proteins were revealed by streptavidin-Alexa fluor 647. **(E-F)** Controls in 5XFAD mice showed **(E)** omit H_2O_2 markedly reduced biotinylation, while **(F)** omit primary and secondary antibodies abolished biotinylation. Scale bar = 5 μm. **G.** Streptavidin-HRP western blot demonstrates efficient streptavidin bead pulled-down of biotinylated proteins, including the protein bait, PLD3. Protein pull-down efficacy is antibody, biotin-xx-tyramide and H_2O_2 dependent. See also **Figure S1**.

Figure 2. Proteomic analysis of plaque-associated axonal spheroids in AD humans and mice

A. Pipeline of PAAS proteomic analysis. **B.** Experimental design, protein detection and statistical cutoffs. **C.** Venn diagram showing proteomic hits in humans and mice. **D-E.** Volcano plots showing proteins (representing by their gene names) that passed the cutoffs for PAAS proteomes (pink dots) in **(D)** mice and **(E)** humans. Top proteomic hits with the lowest p value are indicated by large pink dots. Large magenta dots indicate proteins previously known to be enriched in PAAS. Asterisk denotes APP was manually added in **(E)**, owing to its exclusion by the proteomic filters. (See **Table S3** for the information about spectra counts.) **F-G.** Gene Ontology analysis shows ranked biological processes and cellular component terms from the PAAS proteomes in humans and mice. See also **Figure S2**.

Figure 3. Protein-protein interaction network and signaling pathway analysis uncover the molecular architecture of PAAS

A. Protein-protein interaction network analysis of the human PAAS proteome. MCODE clustering was performed with protein-protein interaction scores from the String database. Each subcluster was further annotated by Webgestalt and named with the top KEGG pathway. Each edge (grey line) represents protein-protein interactions, and the thickness of the grey line represent protein interaction confidence. Each node represents a protein and the node size was based on fold change while node color was based on p value. **B.** Subclusters in A displayed in color-coded format. **C.** Red nodes (left panel) indicate shared proteins between humans and mice; and (right panel) proteins previously known to be enriched in PAAS. **D.** IPA pathway analysis of the PAAS proteome in humans, showing ranked pathways. Dotted line indicates p = 0.05. **E.** Schematic of the molecular architecture of human PAAS. Our PAAS proteome reflects the accumulation of a variety of subcellular organelles, such as lysosome, phagosome, endosome and endoplasmic reticulum, as well as ubiquitin-proteosomes and cytoskeletal elements. We uncovered many new proteins (red and black) (**Table S2**), such as endolysosomal proteins, stress granule assembly proteins, transmembrane proteins and receptors; and signaling pathways, such as calcium signaling and mTOR signaling. Subsets of new proteins were further validated by immunofluorescence confocal imaging (red) **(Figure S3-2** and **Figure 4, S4** and **Table S2)**. We also identified proteins previously known to be enriched in PAAS (blue)(**Table S2**), such as lysosomal proteins LAMP1, Cathepsin B and D, RAGC [13], PLD3 [39, 40]; autophagosome protein ATG9A and endoplasmic reticulum protein RTN3 [71]; cytoskeletal neurofilament protein [72], microtubule TUBB3 [18];

synaptic proteins Synaptophysin [4] and VAMP2 [13] and Ubiquitin [54, 71]. See also **Figure S3-1 and S3-2**.

Figure 4. mTOR signaling is enriched in axonal spheroids and phosphorylated mTOR is a marker of advanced Alzheimer's pathology

A. Immunofluorescence confocal imaging validation of selected proteomic hits reveals that PI3K/AKT/mTOR signaling molecules, PIK3R4, AKT1, mTOR, LAMTOR, RAGA, RAGC, RHEB, RAPTOR, are enriched within PAAS in both AD humans and mice. To highlight individual PAAS, we used traditional markers Neurofilament SMI312, Cathepsin B (CatB), Cathepsin D (CatD) or Lamp1 according to compatibility of antibody species and staining conditions during co-staining with other markers. (See scale bar in uncropped images in **Figure S4A**.) **B.** Phosphorylated-mTOR-S2448 (red) is highly enriched within PAAS (grey, SMI312) around amyloid plaque (blue, ThioflavinS) in severe AD. Scale bar = 5 μm. **C.** Quantification of mean fluorescence intensity levels of p-mTOR-S2448 within axonal spheroid halos normalized to background fluorescence, comparing severe AD (intermediate to high AD neuropathology, n = 13 patients) versus no/mild AD (no or low AD neuropathology, n = 9 patients). Unpaired t test with Welch's correction, two-tailed, ****, $p < 0.0001$. Black dashed line indicates the median. **D.** A Receiver Operating Characteristic (ROC) curve shows that p-mTOR-S2448 can serve as a hallmark to separate severe AD versus no/mild AD brains. Area under the ROC curve = 0.966, standard error = 0.034, 95% confidence interval = 0.900 to 1.000, p value = 0.0003. See also **Figure S4**.

Figure 5. Human iPSC-derived AD model demonstrates that mTOR signaling inhibition reduces PAAS pathology

A. Workflow of iPSC modeling to recapitulate axonal spheroid pathology around amyloid plaques in human neurons. Human iPSCs are plated at day 0 to generate NGN2 human neurons. Human primary astrocytes are seeded at day 10, followed by 3 to 6 months of co-culture. Oligomerized amyloid beta 1-42 peptides are administered for 7 days to the neuron-glia co-culture to recapitulate PAAS pathology. **B.** Confocal deconvolved image shows formation of a robust axonal spheroid pathology (grey, SMI312) in human neurons, expressing classical autophagosome ATG9A protein (red), around amyloid plaque deposits (blue, ThioflavinS) resembling the postmortem AD brain. **C.** mTOR signaling molecules (red) are expressed in human iPSC-derived axonal spheroids (grey, SMI312). **D-E.** Torin1 treatment inhibited mTOR signaling. **(D)** Immunofluorescence confocal imaging showed that Torin1 reduced p-mTOR-S2448 fluorescence intensity within axonal spheroids. **(E)** Quantification of p-mTOR-S2448 mean fluorescence intensity within individual spheroids. Each dot represents a region of interest (ROI), with axonal spheroids around a thioflavin S labeled plaque. Torin1 treatment group n = 39 and vehicle group n = 38 ROIs, respectively. Unpaired t test, two-tailed, *, $p = 0.019$. **F-K.** Torin1 treatment reduced axonal spheroid pathology in iPSC-derived human neurons. **(F)** Immunofluorescence confocal deconvolved images showed that Torin1 reduced axonal spheroid (grey, SMI312) pathology around amyloid plaques (blue, ThioflavinS). **(G)** Quantification of the percentage of axons with spheroids relative to the total number of axons around amyloid plaques. Ratio paired t test, two-tailed, **, $p = 0.005$. **(H)** Quantitative analysis of axonal spheroid size. Ratio paired t test, two-tailed, *, $p = 0.021$. For G and H, each dot represents the average of 20 to 30 ROIs around plaques obtained from 2 cell culture wells in independent experiments. **(I)** Quantification of axonal spheroid number around individual amyloid plaques. Unpaired t test, two-tailed, **, $p = 0.008$. **(J)** Quantification of axon number around an amyloid plaque in each ROI. For I and J, each dot represents an ROI around an

individual amyloid plaque. Torin1 treatment group n = 56, vehicle group n = 55 ROIs, derived from three independent experiments. Unpaired t test, two-tailed, p = 0.319. **(K)** Quantification of neuronal soma size (related to **Figure S5G**). Each dot represents an individual neuronal soma. Torin1 treatment group n = 298, vehicle group n = 316, derived from three independent experiments. Unpaired t test, two-tailed, p = 0.618. See also **Figure S5**.

Figure 6. mTOR signaling inhibition reduces axonal spheroid pathology *in vivo*

A. Schematic of neuronal specific conditional knockout of *Mtor* in heterozygous floxed mouse. **B-C.** Immunofluorescence confocal images showing neuronal specific Cre-mediated *Mtor* homozygous knockout **(B)**, and heterozygous knockout **(C)** in *Mtor*-floxed mice using AAV9-hSyn-Cre-2A-tdTomato, or AAV PHPeB-Cre-EGFP, respectively. (**B**) mTOR expression (grey) was absent in Cre expressing neurons (red), compared to the adjacent neuron (green, NeuN) without Cre expression. (**C**) mTOR expression (red) was reduced in Cre expressing neurons (green), compared to other neurons (grey, NeuN) without Cre expression. Scale bar 5 μm. **D.** Experimental design of virally-mediated genetic manipulation to study the impact of *Mtor* heterozygous knockout on individual axonal spheroids**. E.** Immunofluorescence confocal images showing AAV9-hSyn-Cre-2A-tdTomato sparsely labeling individual axonal spheroids (red) within a spheroid halo (Lamp, grey). **F.** Quantification showing that AAV9-mediated *Mtor* heterozygous knockout in *Mtor*-flox-5XFAD mice significantly reduced the size of individual axonal spheroid. Each dot represents an animal (n = 5 in each group). Unpaired t test, two-tailed, *, p = 0.027. **G.** Using the same results in (**F**), quantification analysis shows that *Mtor* heterozygous knockout significantly reduced the percentage of larger axonal spheroids (area greater than 10 μm^2). Unpaired t test, two-tailed, *, p = 0.03. **H.** Experimental design of virally-mediated genetic manipulation to study the impact of *Mtor* heterozygous knockout on the whole axonal spheroid halo. **I.** Quantification showing that AAV.PHPeB-mediated *Mtor* heterozygous knockout in *Mtor* -flox-5XFAD mice significantly reduced size of axonal spheroid halos. Each dot represents an animal (n = 3 in each group). Unpaired t test, two-tailed, *, p = 0.041. **J.** Using the same results as in (**I**) and quantified by axonal spheroid halo. Each dot represents an axonal spheroid halo. Knockout group n = 66 and control group n = 109 halos. Experiments repeated three times. Unpaired t test, two-tailed, ****, p < 0.0001. **K.** AAV PHPeB-hSyn-cre-EGFP mediated *Mtor* heterozygous knockout did not alter neuronal soma size. Each dot represents an animal (n = 3 in each group). Unpaired t test, two-tailed, p = 0.90. See also **Figure S6**.

SUPPLEMENTARY FIGURE LEGEND

Figure S1. Proximity labeling of proteins within PAAS in postmortem brain of humans and mice, related to Figure 1

A. Information of human postmortem brains used for PAAS proteomics with details on sample number, age, sex, post-mortem interval (PMI) and neuropathology ABC score. **B.** Representative low zoom images of a large field of view showing amyloid plaques (grey, ThioflavinS positive) in postmortem brains of humans and mice. **C-F.** Controls for proximity labeling in postmortem brains. Proximity labeling of **(C)** PAAS in 5XFAD mouse using LAMP1 as protein bait; and **(D)** PLD3 proximity labeling in neuronal soma of wildtype mouse; **(E)** using a NeuN antibody to biotinylate endogenous neuronal soma proteins. All panels show detection of biotinylated proteins with streptavidin labeling, demonstrating the cellular and subcellular specificity of the reaction. **(F)** Control in 5XFAD mouse shows when no biotinylation reaction was performed, there was no streptavidin labeling, demonstrating the chemical specificity of the reaction and the presence of very low background. Scale bar = 5 μm. **G.** Confocal deconvolved image shows that PLD3 is highly expressed in PAAS (grey, PLD3 labeled) around amyloid plaque (blue, ThioflavinsS labeled), but not in microglia (red, IBA1 labeled) nor in astrocytes (green, S100b labeled). **H.** Comparison of PLD3 expression level in PAAS versus neuronal soma and other neuronal branches outside PAAS in postmortem AD human brains, indicating the majority of PLD3 expression was contributed by PAAS. **I.** Optimization of protein lysis protocol for fixed postmortem brains. The protein lysis buffer (100mM Tris-HCL plus 2% SDS) extracted proteins more efficiently compared to previous published method (PBST plus 2% SDS)[44], as indicated by a blot of housekeeping protein GAPDH and the Coomassie blue gel of the same membrane. **J.** Western blot showing biotinylated proteins pulled down from an anti-NeuN antibody proximity labeled sample. Biotinylated proteins, including the protein bait NeuN, were detected in input brain lysates and streptavidin bead elutes, detected by streptavidin-HRP, but not in the supernatant from bead washes nor in the beads themselves after elution. Although the bait proteins were also detected in the unbound protein fractions, no streptavidin signal was detected from the unbound proteins, indicating that there were a portion of endogenous protein baits that were not biotinylated, yet most of the biotinylated proteins were pulled down efficiently. **I-J.** Uncropped western blot membranes of **(I)** PLD3 pulled down, related to **Figure 1G**, and **(J)** NeuN pulled down, related to **Figure S1H**.

Figure S2. Additional statistic and bioinformatic analysis of PAAS proteomics data from AD human and mice, related to Figure 2

A-B. Correlation analysis among biological replicates of **(A)** human and **(B)** mouse proteomic data. **C-D.** Principal component analysis (PCA) of **(C)** human and **(D)** mouse proteomes after applying a cutoff. **E.** Gene Ontology analysis of proteomic hits detected in the anti-PLD3 proximity labeling that did not pass the threshold after applying the cutoff. Rankings are indicated followed by each term. **F.** Gene Ontology analysis of anti-NeuN proximity labeling neuronal soma proteome after applying cutoff. Rankings are indicated followed by each term.

Figure S3-1: Protein network and pathway analysis uncover molecular architecture of axonal spheroids around amyloid plaques, related to Figure 3

A. Protein-protein interaction network analysis of mouse PAAS proteome. MCODE clustering was performed with protein-protein interaction scores from String database. Each subcluster was

further annotated by Webgestalt and named with the top GO molecular function terms. Each edge represents protein-protein interactions, and the thickness of the grey line represent protein interaction confidence. Each node represents a protein, the node size was based on fold change and node color was based on p value. **B.** Protein-protein interaction subclusters were color-coded. **C.** IPA pathway analysis of PAAS proteomes in 5XFAD mice. Rankings are indicated followed by each term. Dotted line indicates p = 0.05. **D-H.** Selected signaling pathways derived from the IPA pathway analysis of human PAAS proteome (related to **Figure 3D**). For phagosome maturation and synaptogenesis signaling see details in Table S3. The length of bars is based on p value and the color is based on fold change. **I-J.** Gene Set Enrichment Analysis (GSEA) of **(I)** KEGG pathway and **(J)** Reactome of the human PAAS proteome. Rankings are indicated followed by each term. **K.** Detected proteins from GWAS AD risk genes that were found in the human PAAS proteome.

Figure S3-2: Immunofluorescence confocal imaging validation highlights selected proteins expressed in PAAS, related to Figure 3E.

Subsets of proteins previously unknown to be in PAAS (red color-coded proteins from **Figure 3E**), were further validated by confocal immunofluorescence imaging in tissues from humans (A-O) and mice (P-R). These include: **(A-B)** lysosomal proteins GAA and GBA; **(C)** phagosome marker ATP6V0A1; **(D)** fusion and endocytosis protein Synaptotagmin 11 (SYT11); **(E-F)** actin cytoskeleton signaling protein RAC1 and SPTBN1; **(G-K)** calcium signaling and calcium ion channel proteins CAMK2, ATP2B3, Calmodulin1, CACNA1B and CACNA1D1; **(L-O)** stress granule proteins G3BP1 and G3BP2; mTOR signaling (see details in **Figures 4 and S4**); as well as **(M-N)** transmembrane protein and receptor ITM2B and NTRK2. We identified some proteins that are highly expressed in PAAS in AD humans, such as (**D**) SYT11 and **(L-O)** G3BP1 and G3BP2, but not in 5XFAD mice. On the other hand, calcium signaling protein CAMK2 is highly expressed in 5XFAD mice but is expressed at intermediate to low level in AD humans **(G and R)**. In addition, the lysosomal proteins (**P**) GAA and **(Q)** TPP1 were highly enriched in the core of many axonal spheroids in 5XFAD mice, similar to the previous reported tau core [73]; whilst in AD humans, the "core" distribution of these two proteins were rarely observed **(A-B)**. Confocal images were deconvolved.

Figure S4. mTOR signaling is enriched within axonal spheroids, related to Figure 4

A. Original uncropped images of **Figure 4A**. Immunofluorescence confocal imaging showing that PI3K/AKT/mTOR signaling molecules, PIK3R4, AKT1, mTOR, LAMTOR, RAGA, RAGC, RHEB, RAPTOR, are enriched within PAAS in both AD humans and mice. Scale bar = 5 μm. **B.** mTOR expression in human AD, MCI, and 5XFAD mice. mTOR (red) is enriched in axonal spheroids (grey, SMI312 positive) of AD and MCI patients. In young 5XFAD mice at around 2 to 4-month-old, mTOR is enriched in axonal spheroids, while in older 5XFAD mice at around 12 to 15-month-old, mTOR expression within PAAS is equivalent or lower compared to that in the tissue around spheroids. Scale bar = 5 μm.

Figure S5. mTOR signaling inhibition reduces axonal spheroid pathology in iPSC-derived human neurons, related to Figure 5

A. Immunofluorescence confocal deconvolved image showing iPSC-derived human neurons (red, neurofilament H) robustly expressing pre- and post-synaptic markers (green, Synapsin1/2; grey, PSD95) at around day 150 of co-culture. **B.** Immunofluorescence confocal image showing the presence of both neurons (grey, SMI312) and astrocytes (red, S100b) in the co-culture. **C.**

Immunofluorescence confocal image showing 6e10 positive (grey) and ThioflavinS positive (blue) amyloid beta deposits and neuronal branches (NFH in red) in human iPSC-derived neuron-glia co-cultures) treated with amyloid beta 1-42 peptides, but not in untreated controls. **D.** Immunofluorescence confocal deconvolved images of AAV2-CB7-GFP infected human neurons that formed axonal spheroids, as revealed by anti-GFP staining (green) and co-stained with the axonal spheroid marker SMI312 (grey), showing SMI312 is a good marker for measuring spheroid size. **E.** Immunofluorescence confocal deconvolved images showing phosphorylated Tau S235, S396 and S404 (red) was expressed in iPSC-derived human neurons, including in axonal spheroids (grey, SMI312) around amyloid plaques (blue, ThioS). **F.** Original uncropped images of Figure 5C. mTOR signaling molecules (red) expressed in human iPSC-derived axonal spheroids (grey, SMI312) around amyloid plaques (blue, ThioS). **G.** Immunofluorescence confocal images of AAV2-CB7-GFP infected human neurons. Neuronal cell bodies were revealed by both anti-GFP (green) and anti-NeuN (grey) staining, related to **Figure 5K**.
H. Quantification of amyloid plaque size by measuring the area of an individual amyloid plaque within the imaged ROI. Each dot represents an amyloid plaque. Torin1 treatment group n = 201, vehicle group n = 253. Experiments repeated three times. Unpaired t test, two-tailed, p = 0.419.

Figure S6. mTOR signaling inhibition reduced axonal spheroid pathology *in vivo*, related to Figure 6

A. Uncropped immunofluorescence confocal images showing AAV9-hSyn-cre-2A-tdTomato-mediated *Mtor* complete knockout in homozygous *Mtor*-flox-5XFAD mice. mTOR expression (grey) was absent in Cre expressing neurons (red), compared to other adjacent neurons (green, NeuN) without Cre expression. **B.** AAV PHPeB-hSyn-cre-EGFP-mediated mTOR heterozygous knockout in heterozygous mTOR-flox-5XFAD mice. mTOR expression (red) was reduced in Cre expressing neurons (green), compared to other adjacent neurons (grey, NeuN) without Cre expression. **(A-B)** scale bar = 5 μm. **C.** Immunofluorescence confocal images showing AAV PHPeB virus (green) infection efficiency in somatosensory cortex of 5XFAD mice. Anti-NeuN staining (red) indicated neuronal cell bodies. **D.** Representative confocal images of axonal spheroids halo (grey, Lamp1) around amyloid plaques (blue, ThioS) in AAV PHPeB-hSyn-cre-EGFP-mediated *Mtor* heterozygous knockout mice. **E.** Immunofluorescence confocal image showing NeuN (red) positive neuronal soma (green, AAV PHPeB-CAG-EGFP infected) used for soma size quantification. **F.** Quantification of amyloid plaque size by measuring the area of individual amyloid plaques within each ROI. Each dot represents an amyloid plaque. Experimental group n = 66, control group n = 109. Experiments repeated three times. Unpaired t test, two-tailed, p = 0.581. **G-I.** Quantification of expression level of autophagy marker LC3B, as well as mRNA local translation regulator phosphorylated-P70S6K-Thr389 and its total protein, by measuring the fluorescence intensity of each protein within AAV PHPeB virus infected neuronal cell bodies in each ROI. Each dot represents an animal (n = 3 in each group). Experiments repeated three times. Paired t test, two-tailed. **(I)** *, p = 0.012; **(J)** *, p = 0.015; **(K)** p = 0.287.

METHODS

Human postmortem brain tissue

Snap frozen postmortem human brain specimens of frontal cortices from AD patients and age-matched controls were obtained from the Yale Alzheimer's Disease Research Center and the Banner Sun Health Research Institute. Detailed demographic and clinical information can be found in **Figure S1** and **Table S1**. For proximity labeling proteomics, three AD cases with high Neuropathologic Changes score [48]: A2-3, B3, C2-3 and three age-matched controls ((Neuropathologic changes score: A0-1, B1, C0) were used. To reduce inter-sample variability and maximize signal-to-noise by avoiding brains with low-density amyloid deposition, we carefully inspected ~20 individual postmortem brains using microscopy and selected for proteomic analysis the top 3 AD brains with the highest density of amyloid plaques and axonal spheroids within the frontal cortex. For immunofluorescence proteomic validations, 13 severe AD cases and 9 no/mild AD cases were used.

Human iPSC line and human primary astrocytes

A de-identified control human iPSC line NSB3182-3 (female) was used in all experiments, fully characterized [74]. *NGN2*-induced glutamatergic neurons [43] were generated and co-cultured with human primary astrocytes (ThermoFisher #N7805200) for all experiments [44].

Mice

All animal procedures were approved by the Institutional Animal Care and Use Committee at Yale University. WT (C57BL/6J), 5XFAD (Tg6799) mice [75] and mTOR-flox (JAX #011009) mice [47] were obtained from Jackson Laboratory. 5XFAD and WT mice, used for proximity labeling proteomics, were euthanized at 15-month-old, followed by transcardial perfusion. Three male mice per genotype (WT and 5XFAD) were used. Animals used for immunofluorescence proteomic validation were euthanized at 2-3 or 12-15 months of age, with 3 biological replicates per experiment. mTOR-flox mice were cross-bred with 5XFAD mice to create an mTOR-flox-5XFAD line. For AAV mediated mTOR heterozygous knockout experiments, mTOR-flox-5XFAD mice were injected with AAVs at 6 weeks of age. Five biological replicates (combining male and female mice) in each group were used for AAV9-hSyn-cre-2a-tdT experiment, and 3 male mice in each group were used for AAV-PHPeB experiment.

Antibodies and reagents

Full list of primary antibodies for known and newly validated PAAS proteins can be found in **Table S2**, including catalog number, RRID, dilution factors and brief staining instructions. Briefly, Anti-PLD3 antibody, anti-SMI312 and anti-Cathespin D were used to label PAAS in both mice and humans. Anti-Lamp1 and anti-Cathespin B antibodies were used to label PAAS in mice. For proteomic hits validation, anti-GAA, anti-GBA, anti-TPP1, anti-ATP6V0A1, anti-SYT11, anti-G3BP1, anti-G3BP2, anti-ITM2B, anti-SPTBN1, anti-SV2A, anti-ATP2B3, anti-CAMK2A, anti-Calmodulin, anti-SYT1, anti-CACNA2D1, anti-CACNA1B, anti-NTRK2, anti-mTOR, anti-p-mTOR S2448, anti-PIK3R4, anti-AKT1, anti-LAMTOR, anti-RAGA, anti-RAGC, anti-RHEB, anti-RAPTOR were used for validating newly identified PAAS proteins. Anti-RAGC, anti-ATG9A, anti-Ubiquitin, anti-RTN3, anti-PKC, anti-synaptophysin, anti-SNAP25, anti-VAMP2, anti-beta Tubulin III, anti-LC3B were used for immunostaining of known PAAS proteins. To reveal GFP and tdTomato protein expression, anti-GFP (1:500, RRID:AB_10000240) and anti-RFP (1:200, RRID:AB_2209751) were used respectively. For staining neuronal and glial markers

in iPSC-derived human neurons, anti-neurofilament H (1:1000, RRID:AB_2149761), anti-NeuN (1:1000, RRID:AB_10711040), anti-NeuN (1:200, RRID:AB_2532109), anti-Synapsin1/2 (1:500, RRID:AB_2622240), anti-PSD95 (1:200, RRID:AB_10807979), anti-S100b (1:500, RRID:AB_2814881), anti-IBA1 (1:100, RRID:AB_2891289) were used. To stain amyloid beta deposits, anti-6e10 (1:200, RRID:AB_2565328) was used. To stain phosphorylated Tau, anti-phospho-Tau S235 (1:1000, Thermo-Fisher), anti-phospho-Tau S396 (1: 200) and anti-phospho-Tau S404 (1:200) were used (RRID see **Table S2**). Dendritic marker MAP2 (1:200, RRID:AB_776174) was used. Thioflavin S (Sigma-Aldrich, T1892, 2% w/v stock solution, 1:10k staining) was used to label amyloid plaques. Alexa dye conjugated secondary antibodies were used (1:600, ThermoFisher Scientific).

Tissue fixation

We have compared the impact of different tissue fixation approaches on the proximity labeling efficacy and protein extraction efficiency. For human brain samples, snap frozen postmortem human brains coupled with fresh fixation in 4% PFA at 4 °C for ~24 hours worked the best; for mice, freshly perfused mouse brains and fixed in 4% PFA at 4 °C for ~24 hours performed the best in both proximity labeling efficacy and protein extraction efficiency. We found that long term fixation and storage with FFPE markedly reduced both proximity labeling and protein extraction efficiencies.

Proximity labeling in brain tissue

Proximity labeling in human and mice tissue was performed based on [35] with optimizations. Axonal spheroids were proximity labeled by using anti-PLD3 antibodies in both mice and humans. Neuronal soma were proximity labeled using anti-NeuN antibody. Briefly, frozen postmortem human brain specimens were fixed by submerging into ice cold 4% paraformaldehyde, and put onto a shaker at 4 °C for ~ 24 hours. For mice, after transcardial perfusion, brains were fixed in 4% paraformaldehyde at 4 °C for ~ 24 hours while shaking. Human and mouse brains were vibratome sectioned at 50 μm thickness. Ten sections (around 1cm x 0.8cm each) for human or mouse brain were used in each reaction/per biological replicate. Human sections contained mostly grey matter. Three biological replicates were used in each group. Sections were permeabilized by PBS with 0.5% Triton X-100 for 7 min, followed by rinsing with PBST (0.1% Tween-20 in PBS). To quench the endogenous peroxidase activity, sections were incubated in 0.1% H_2O_2 for 10 min, followed by rinsing with PBST twice. Primary antibody diluted in blocking buffer (0.1% Tween-20 with 1% BSA in PBS) was incubated overnight at 4 °C on a shaker, followed by PBST washes for 3 times 20 min/per wash. Secondary antibody conjugated with HRP was incubated in blocking buffer for 1 hour at room temperature, followed by PBST washes for 3 times ~40 min/per wash. Proximity labeling was performed by using Biotin-XX-Tyramide (ThermoFisher Scientific) dissolved in 50 mM Tris-HCl buffer (pH = 7.4), with H_2O_2 for 5 min. Biotinylation reactions were terminated by rinsing sections with freshly made 500 mM sodium ascorbate for 3 times, followed by PBST washes for 3 times.

Enrichment of biotinylated proteins

We performed proximity labeling proteomics on fixed brain specimens, which may reduce the protein extraction yield compared to other proximity labeling methods using fresh tissue. Thus, we optimized the protein extraction protocol and largely increased the protein extraction yield compared to previously published methods (**Figure S1I**)[35]. Specifically, brain sections from proximity labeling experiments were lysed and de-crosslinked in 100 mM Tris-HCl buffer (pH =

8.0) with 2% SDS and protease inhibitor (Roche) at 95 °C for 45 min with constant shaking. For every 10 brain sections, 500uL lysis buffer was used. Protein lysate was sonicated using Sonic Dismembrator Model 500 (Fisher Scientific) for 3 times, 3 sec/per time at 4°C. Protein lysate was centrifuged at 12k rcf for 5 min. Then, 450 µL protein lysate supernatant was collected from each sample, incubated with 550 µL of PBST containing 200 µL prewashed streptavidin magnetic beads (ThermoFisher Scientific), protease inhibitor and phosphatase inhibitor, to meet a final 1mL volume. Samples were then incubated on a 360° rotator at 4 °C overnight. The rest of protein lysate were used for protein concentration measurement by BCA (ThermoFisher Scientific). After incubation, beads were sequentially washed once with PBST, twice with PBST with 1 M NaCl, twice with PBS. Biotinylated proteins were eluted in elution buffer (20 µL of 20 mM DTT and 2 mM Biotin in 1X NuPAGE LDS lysis buffer (ThermoFisher) with protease inhibitor and phosphatase inhibitor) at 95 °C for 5min. Supernatant was collected and centrifuged at 12k rcf for 1min, followed by running into a 4%–20% Tris-Glycine gel (Invitrogen) at constant 150 V until all the proteins had run into the gel (approximately 10min). Gel was rinsed once in ultrapure water (AmericanBio) and incubated in ~50 mL of Coomassie blue R-250 staining solution (Bio-Rad) for 1 hour incubation. Gel was de-stained with Coomassie blue R-250 destaining solution (Bio-Rad) for 2 hours with 3 times buffer changes. Gel was rinsed with ultrapure water for three times. Gel containing protein samples was visualized, cut with clean blades, and kept at -20 °C.

Western blotting

For western blot, 4%–20% Tris-Glycine gels (Invitrogen) were used for protein electrophoresis following the manufacturer's protocol. Proteins were transferred to nitrocellulose membranes (BioRad) at constant 350 mA for about 50 min. After blocking with 5% bovine serum albumin (BSA) in TBST (Tris-buffered saline with 0.1% Tween 20) for 1 hour, membranes were incubated with primary antibodies (anti-PLD3 1:250; anti-NeuN 1:1000; anti-GAPDH 1:1000) diluted in 5% BSA in TBST on a shaker at 4 °C overnight, followed by three times of 15min washes with TBST. Membranes were then incubated with horseradish peroxidase (HRP) conjugated secondary antibodies diluted in 5% BSA in TBST for 1 hour at room temperature, followed by three times of 15min washes with TBST. To blot biotinylated proteins on the same membrane, stripping buffer (ThermoFisher #46430) was used to cover the whole membrane and incubated at room temperature with shaking for 10-12 min, followed by rinsing with PBST for 3 times. HRP-conjugated streptavidin (1:1000) was diluted in blocking buffer for 1-2 hours at room temperature or 4 °C overnight. Clarity Western ECL blotting substrate (Bio-Rad) and ChemiDoc MP imaging system (Bio-Rad) were used for chemiluminescence development and detection.

In-Gel Digestion

Gel slices were cut into small pieces and washed with 600 µL of water on a tilt-table for 10 minutes followed by 20 min wash with 600 µL 50% acetonitrile (ACN)/100 mM NH4HCO3 (ammonium bicarbonate, ABC). The samples were reduced by the addition of 100 µL 4.5 mM dithiothreitol (DTT) in 100 mM ABC with incubation at 37ºC for 20 min. The DTT solution was removed and the samples were cooled to room temperature. The samples were alkylated by the addition of 100 µL 10mM iodoacetamide (IAN) in 100 mM ABC with incubation at room temperature in the dark for 20 min. The IAN solution was removed, and the gels were washed for 20 min with 600 µL 50% ACN/100 mM ABC, then washed for 20 min with 600 µL 50% ACN/25 mM ABC. The gels were briefly dried by SpeedVac, then resuspended in 100 µL of 25mM ABC containing 500 ng of digestion grade trypsin (Promega, V5111), and incubated at 37ºC for 16 hours. The supernatants

containing the tryptic peptides were transferred to new Eppendorf tubes. Residual peptides in the gel bands were extracted with 250 µL 80% ACN/0.1% trifluoroacetic acid (TFA) for 15 min, then combined with the original digests and dried in a SpeedVac. Peptides were dissolved in 24 µL MS loading buffer (2% acetonitrile, 0.2% trifluoroacetic acid), with 5 µL injected for LC-MS/MS analysis.

LC-MS/MS on the Thermo Scientific Q Exactive Plus

LC-MS/MS analysis was performed on a Thermo Scientific Q Exactive Plus equipped with a Waters nanoAcquity UPLC system utilizing a binary solvent system (A: 100% water, 0.1% formic acid; B: 100% acetonitrile, 0.1% formic acid). Trapping was performed at 5 µL/min, 99.5% Buffer A for 3 min using an ACQUITY UPLC M-Class Symmetry C18 Trap Column (100Å, 5 µm, 180 µm x 20 mm, 2G, V/M; Waters, #186007496). Peptides were separated at 37 °C using an ACQUITY UPLC M-Class Peptide BEH C18 Column (130Å, 1.7 µm, 75 µm X 250 mm; Waters, #186007484) and eluted at 300 nL/min with the following gradient: 3% buffer B at initial conditions; 5% B at 2 min; 25% B at 140 min; 40% B at 165 min; 90% B at 170 min; 90% B at 180 min; return to initial conditions at 182 min. MS was acquired in profile mode over the 300-1,700 m/z range using 1 microscan, 70,000 resolution, AGC target of 3E6, and a maximum injection time of 45 ms. Data dependent MS/MS were acquired in centroid mode on the top 20 precursors per MS scan using 1 microscan, 17,500 resolution, AGC target of 1E5, maximum injection time of 100 ms, and an isolation window of 1.7 m/z. Precursors were fragmented by HCD activation with a collision energy of 28%. MS/MS were collected on species with an intensity threshold of 1E4, charge states 2-6, and peptide match preferred. Dynamic exclusion was set to 30 seconds.

Peptide Identification

Data was analyzed using Proteome Discoverer software v2.2 (Thermo Scientific). Data searching was performed using the Mascot algorithm (version 2.6.1) (Matrix Science) against the SwissProtien database with taxonomy restricted to human (20,368 sequences) or mouse (17,034 sequences) as well as a streptavidin sequence. The search parameters included tryptic digestion with up to 2 missed cleavages, 10 ppm precursor mass tolerance and 0.02 Da fragment mass tolerance, and variable (dynamic) modifications of methionine oxidation and carbamidomethyl cysteine. Normal and decoy database searches were run, with the confidence level set to 95% ($p<0.05$). Scaffold v5.1.2 (Proteome Software Inc., Portland, OR) was used to validate MS/MS based peptide and protein identifications. Peptide identifications were accepted if they could be established at greater than 95.0% probability by the Scaffold Local FDR algorithm. Protein identifications were accepted if they could be established at greater than 99.0% probability and contained at least 2 identified peptides (one uniquely assignable to the protein). Proteins that contained similar peptides and could not be differentiated based on MS/MS analysis alone were grouped to satisfy the principles of parsimony. Proteins sharing significant peptide evidence were grouped into clusters. Label-free quantification was performed with Scaffold software. Spectral intensity values were used for protein quantification between groups.

Proteomic data analysis

To obtain the PAAS proteome, differentially expressed proteins were analyzed by comparing proteomic hits obtained from PLD3-labeled samples versus those from control samples using no antibody. This allowed filtering of endogenously biotinylated proteins and non-specific binders to

streptavidin beads. To obtain the optimal cutoff values for the statistical analysis we tested different degrees of stringency for FDR (0.1, 0.05 and 0.01) and fold change (1 and 1.5). An optimum cutoff $p < 0.05$, FDR < 0.1 and fold change > 1 was used for these datasets, as it captures the maximum numbers of known PAAS proteins while excluding the maximum numbers of potential contaminants. A pseudo-spectra count of 0.1 was added to all spectra values before calculating the fold changes between experimental samples and controls [76]. Post-cutoff proteomic lists were scrutinized for possible glial contaminations by cross validations using single cell RNAseq (scRNAseq) transcriptomics in mice and humans [77] and Tissue Atlas in The Human Protein Atlas [78]. When a gene had an FPKM < 10 in neurons and an FPKM > 10 in other cell types in the scRNAseq datasets [77], and protein expression was not detected in neurons from the Tissue Atlas [78], this gene was excluded from the proteomic results.[78]. One such gene (TNS3) was excluded from the PAAS proteome in AD humans, and five such genes (Gsn, Ephx2, Gfap, Myh9 and Anxa2) were excluded from the PAAS proteome in AD mice. Proteomic hits that passed these thresholds were considered the final PAAS proteomes in AD humans or mice. For principal component analysis (**Figures S2C-D**), raw proteome data from PLD3-labeled and no antibody control samples were imported into Qlucore Omics Explorer v3.6 (Qlucore AB, Lund, Sweden). Two group comparison between PLD3 labeled and no antibody control samples was performed. A cutoff of $p < 0.05$ and FDR < 0.1 was applied before principal component analysis. Full lists of raw proteomic hits and filtered PAAS proteomes of AD humans and mice can be found in **Table S3**.

For gene ontology analysis (**Figures 2F-G, S2E-F**), we uploaded the final proteomes to the ToppGene Suite search portal [79] and plotted the top five or top twenty retrieved terms on cellular compartment or biological process with the lowest false discovery rates. For the protein-protein interaction network (**Figures 3A-C and S3-1A-B**), final proteomes were uploaded into STRING v11.0 search portal [80] to construct protein-protein interaction networks using a medium confidence interaction score 0.4 and plotted in Cytoscape (v3.8.0) [81]. Network clustering was performed using the MCODE [82] plugin in Cytoscape, and the top 8 protein clusters in AD humans were shown in **Figures 3A-B**; top 9 protein clusters in 5XFAD mice were shown in **Figures S3-1A-B**. Full lists of protein-protein-interactions and sub-clusters of PAAS proteomes of AD humans and mice can be found in **Table S3**. Web-based Gene Set Analysis Toolkit (WebGestalt) [83] was used to determine KEGG pathways and gene ontology cellular component for individual protein clusters for AD humans. The top AD related KEGG pathway with the lowest false discovery rate was annotated in **Figures 3A-B** for protein clusters 1-6 and 8, namely endocytosis, synapse, phagosome 1, proteasome, phagosome 2, ubiquitin-mediated proteolysis and glutamatergic synapse. Protein cluster 7 was annotated using the top gene ontology cellular component (ATPase complex), given that no AD related KEGG pathway was observed. Similarly, the top gene ontology molecular function terms were annotated for each protein cluster from 5XFAD mice (**Figures S3-1A-B**). For IPA pathway analysis (**Figures 3D and S3-1C-H**), human PAAS proteome was imported into Ingenuity Pathway Analysis (IPA) software (QIAGEN, 2020 released version)[84] for canonical pathway analysis. The top two IPA pathways (phagosome maturation and synaptogenesis) with the lowest false discovery rates and another five significant IPA pathways with potential relevance to PAAS pathology listed are **Figures 3D** (See also **S3-1C-H and Table S3**). Similarly, IPA pathway analysis was performed for PAAS proteome of 5XFAD mice (**Figures S3-1C and Table S3**). Full lists of IPA pathway analysis of PAAS proteomes in AD humans and mice can be found in **Table S3**. For gene set enrichment analysis (**Figure S3-1I-**

J), PAAS proteome of AD human were uploaded into the Broad Institute GSEA software 4.1.0 [85] to perform KEGG and Reactome analysis using default values. P values, FDR values and normalized enrichment scores were used for ranking.

Immunofluorescence of fixed specimens and human iPSC-derived co-culture

For immunofluorescence of fixed specimens of humans and mice, the complete list of antibodies, dilution factors and immunofluorescence instructions can be found in **Table S2**. Briefly, for mice and human brains, fixation and vibratome sectioning was the same as described in the proximity labeling section. Heat-induced sodium citrate antigen retrieval was performed when necessary (see IF instructions in **Table S2**). Immunofluorescence staining was then performed with the following protocol: tissue was boiled in 50 mM sodium citrate with 0.05% tween-20 at 95 °C for 45 min, followed by 30 min cool down at RT and rinse with PBS for three times. Primary antibodies incubation were 12 hours to 3 days at 4 °C in blocking buffer (PBS with 1% BSA and 0.1% Tween-20) and secondary antibodies were incubated in blocking buffer at 4 °C overnight. Thioflavin S (Sigma-Aldrich, T1892, 2% w/v stock solution, 1:10k staining) was used for labeling amyloid deposits. Three times washes with PBST were performed before mounting tissues on slides with PermaFluor (Thermo Scientific, TA-030-FM).

For immunofluorescence of human iPSC-derived neuron-astrocyte co-culture, cells were washed 3 times with pre-warmed PBS before fixing with 4% PFA (ice-cold) at RT for 20 min. Cells were washed with PBS 15 min x 3 and were blocked with blocking buffer (1% BSA in PBS, plus 0.1% tween-20) for 1 h. Primary antibodies were diluted in blocking buffer and incubated with cells at 4 °C overnight. Cells were washed with PBST 15 min x 3. Secondary antibodies were diluted in blocking buffer and incubated with cells at 4 °C overnight. ThioflavinS (2% w/v stock solution, 1:10k staining) was diluted in PBS and incubated with cells at RT for 5 min. Cells were washed with PBST 15 min x 3, before imaging.

Confocal microscopy

A Leica SP8 confocal microscope was used to generate all images. Laser and detector (the GaAsP hybrid detection system, photon counting mode) settings were maintained constant. For all analyses, single z stack images or tiled images were obtained in somatosensory cortex in mice. All images were obtained using a 63x oil immersion objective (N.A. 1.40), 40x water immersion objective (N.A. 1.10) or 25x water immersion objective (N.A. 0.95) at 1,024 x 1,024 pixel resolution, z-step size of 1 μm, as we previously described [63]. When indicated, deconvolution was performed using the default setting in the Leica SP8 LAS X software.

Lentivirus plasmid purification, lentivirus production and concentration

Escherichia coli stocks for pMDLg/pRRE (MDL), pRSV-Rev (Rev), pCMV-VSV-G (VSVG), FUW-M2rtTA and pLV-TetO-hNGN2-eGFP-Puro were purchased from Addgene (12251, 12253, 8454, 20342 and 79823, respectively). Bacteria was grown in 500 mL of LB Broth (Fisher Scientific, DF0446-07-5) with 100 μg/mL Ampicillin (Sigma, A9518) overnight at 37 °C and 200 rpm. In the following day, bacterial cells were pelleted by centrifugation at 4000 g for 10 min at 4 °C. The supernatant was discarded, and plasmids purified using the PureLink™ HiPure Plasmid Filter Maxiprep Kit (Invitrogen, K210017), following manufacturer instructions.

Third generation lentiviral vectors were produced as we described [86]. Briefly, HEK 293T cells (Invitrogen, R700-07) were grown in 15-cm plates (Falcon, 353025) in DMEM (Gibco, 12430054) supplemented with 10% FBS (Gibco, 10438026) until reaching 70-80% confluency. For cell transfection, the following solution was prepared in 500 µL of pre-warmed Opti-MEM (Gibco, 31985062) per plate: 12.2 µg of transfer plasmid, 8.1 µg of MDL, 3.1 µg of Rev, 4.1 µg of VSVG and 110 µL of Polyethylenimine (1 µg/µL; Polysciences, 23966-2). This solution was incubated for 10 min at room temperature, vortexed gently and added dropwise onto HEK 293T cells for transfection. Medium was changed after 6 h of incubation and harvested at 48 h and 72 h post transfection. Media containing viral particles was sterile-filtered and concentrated using the Lenti-X™ Concentrator (Takara Bio, 631231), according to manufacturer instructions.

Human neuron-astrocyte co-culture AD model

Human iPSC control line 3182-3 was used in this experiment, as we first described this line in [74]. Maintenance and passaging of human iPSC was performed as we previously described [87]. Human primary astrocytes (ThermoFisher #N7805200) were maintained as described in user manual. iPSC-derived NGN2-induced glutamatergic neuron generation was performed as we previously described [87]. Briefly, human iPSCs maintained in 6-well-plates were harvested by incubating in Accutase (Innovative Cell Technologies AT104) 1 mL/per well plus 10 µM ROCK inhibitor THX (RI)(Tocris #1254) at 37 °C for 20 min. Dissociated iPSCs were then collected in a 50 mL falcon tube and mixed well with DMEM (ThermoFisher #11966025)(preferably 1:3 Accutase : DMEM). iPSCs were centrifuged for 4 min at RT at 1000 g. iPSC were resuspended in 1-2 mL of Stemflex (ThermoFisher) with 10µM RI and counted, diluted in Stemflex with THX to a cell suspension concentration of 1e6 cells/mL. Lentiviruses NGN2-Puro and rtTA (titer 4.40 x 10^10 gc/mL) at 50 uL per 10e6 cells of suspension were added. Cells were mixed and dispensed at 120k cells/per well (6 well size) coated with 1x Geltrex (ThermoFisher). Cells were incubated at 37 °C incubator overnight. DIV1: media was replaced with induction media (DMEM F12 with Glutamax and Sodium Pyruvate (Thermofisher, #10565018), 1% N-2 (Thermofisher, #17502048), 2% B-27-RA (Thermofisher, #12587010), Doxycycline for a final concentration of 1ug/mL). DIV2 and 3: replaced media with induction media contained puroymycin (2 ug/mL) on each day. DIV4: Neurons were dissociated with Accutase plus 10 µM RI for 20 min, washed off with 1:3 DMEM, resuspended and centrifuged at 1000 g for 5 min. Resuspend pellet at a concentration of 1e6 cells/ml in neuron media (Brainphys (STEMCELL, # 05790), 1% N-2, 2% B-27-RA, 1 µg/mL Natural Mouse Laminin (Thermofisher, # 23017015), 20 ng/mL BDNF (R&D, #248), 20 ng/mL GDNF (R&D, #212), 250 µg/mL Dibutyryl cyclic-AMP (Sigma, #D0627), 200 µM L-ascorbic acid (Sigma, # A4403) and 1x Anti-Anti (ThermoFisher)) with Dox 1µg/mL, puromycin 2 µg/mL, 4 µM AraC (Sigma #C6645) and 10 µM RI. Neurons were replated onto 2x Geltrex coated 96-well-plates (PerkinElmer #6055302) and seeded at 10e5 per well (96-well plate size). DIV5: media was replaced with neuron medium containing puromycin 2 µg/mL and AraC 4 µM. DIV6: media was replaced with neuron medium with 4 µM AraC. DIV8: media was replaced with neuron medium with 2 µM AraC. DIV10: human primary astrocytes were dissociated with TrypLE (ThermoFisher), washed with DMEM, centrifuged at 400 rcf for 5 min, counted and plated into NGN2 neurons culture at 20k cells/per well (96-well-plate size). Human iPSC-derived neuron-astrocyte co-culture was maintained as previously described [44] with modifications. Briefly, human neuron-astrocyte co-culture were maintained in neuron media plus 1.5% FBS for 1 week, then reduced FBS to 0.5% for another week. Media was half-changed every other day. After that, human neuron-astrocyte co-cultures were maintained in neuron maintenance medium (1X

BrainPhys Basal (StemCell Technology), 1X B27 with Vitamin A (ThermoFisher), 1X N2 (ThermoFisher), 5 μg/ml Cholesterol (Sigma-Aldrich), 1 mM Creatine (Sigma-Aldrich), 10 nM β-estradiol, 200 nM Ascorbic Acid, 1 mM cAMP (Sigma-Aldrich), 20 ng/ml BDNF (Peprotech), 20 ng/ml GDNF (Peprotech), 1 μg/ml Laminin, 0.5 mM Glutamax (ThermoFisher), 1 ng/ml TGF-β1 (Peprotech), 1X Normocin (InvivoGen), 50 U/ml Penicillin- Streptomycin (ThermoFisher)) with half-changed of media every other day until harvest, or other assays. For AD modeling, amyloid beta 1-42 peptide (AnaSpec AS-72216) was oligomerized to prepare soluble amyloid beta species as previously described [44, 60]. Briefly, soluble amyloid beta species were added to the neuron maintenance medium at a final concentration of 5 μM and applied to the human neuron-astrocyte co-culture for 7 days, with half-change of media every other day as previously described [44]. For mTOR signaling inhibition, Torin1 (TOCRIS 4247) or vehicle DMSO was added to the neuron maintenance medium at a final concentration of 250 nM [45], and applied to the human neuron-astrocyte co-culture 3 days before amyloid beta treatment. Then, Torin1 or vehicle DMSO was added to the neuron maintenance medium at 250 nM concentration, along with soluble amyloid beta species at 5 μM concentration, and applied to the human neuron-astrocyte co-culture for 7 days, with half-change of medium every other day.

Viral-mediated *Mtor* heterozygous knockout in *Mtor*-floxed-5XFAD mice

mTOR is known to be a regulator of cell growth [25, 45], previous studies showed cell size was indistinguishable between the *Mtor* heterozygous knockout and wild-type cells [88], which suggests that the effects of *Mtor* knockout on cell size is *Mtor* gene-copy dose dependent. Thus, we obtained *Mtor* heterozygous floxed AD mice to achieve conditional *Mtor* heterozygous knockout, which had no effect on cell body size (**Figures 6K and S6E**). To achieve global neuronal *Mtor* heterozygous knockout in *Mtor*-floxed-5XFAD mice, 10 μL of AAV-PHPeB-hsyn-cre-eGFP (Addgene#105540, titer ~1x10^13) or AAV-PHPeB-CAG-GFP (Addgene#37825, titer ~1x10^13) was retro-orbitally injected into 6-week-old *Mtor*-floxed-5XFAD mice. To achieve sparse neuronal *Mtor* heterozygous knockout, 1 μL of AAV9-hsyn-cre-2a-tdT (Addgene#107738, titer ~1x10^13) was diluted with 3 μL of PBS and was injected into the subarachnoid space of one hemisphere at the level of somatosensory cortex in *Mtor*-floxed-5XFAD mice, as we previously described [63]. Mouse brains were collected 2 months after virus injection in the AAV-PHPeB experiment or at 2.5 months for the AAV9-hsyn-cre-2a-tdT injected mice. Brains were sliced, stained and imaged with confocal microscopy as abovementioned and as we previously described [63].

Image analysis and quantification

All images were taken using Leica SP8 confocal microscopy, and all analyses were processed with FIJI (ImageJ) software, unless otherwise described. For analysis of PLD3 distribution in PAAS versus neuronal soma or neuronal branches outside axonal spheroids, we performed semi-quantification in postmortem brains of three AD humans, which were used for PAAS proteomics. Immunofluorescence staining of PLD3 and thioflavin S staining was performed followed by confocal imaging. PLD3 background signal was measured in each image and a background value ranging from 25-60 was subtracted to remove the noise from the background. Z stack images were then maximum projected. PAAS halos were manually circled, and raw integrated intensity (RawInt) was measured. RawInt was also measured for the whole images. PLD3 expression from PAAS was measured by sum of RawInt from all the PAAS halos, whereas expression from neuronal soma

and other neuronal branches was measured by subtracting RawInt of PAAS from that of the whole image.

For p-mTOR S2448 fluorescence intensity measurement in human AD or no/mild AD postmortem brains, each zoom 1 z-stack image, containing SMI312 positive axonal spheroids around amyloid plaques, were maximum projected. Then, SMI312 positive spheroid halos were circled, and mean fluorescence intensity of the p-mTOR S2448 channel was measured within the selected circle. In the same field of view, regions without spheroids were considered as background. Three such background regions were selected, circled and p-mTOR mean intensity was measured. The three "background" p-mTOR mean intensity from each field of view was averaged. Mean intensity (p-mTOR dystrophy halo) / mean intensity (p-mTOR background) was calculated to represent the p-mTOR expression level in each axonal spheroid halo. Three fields of view were quantified in each severe AD patient, and 1-3 fields of view were quantified in each no/mild AD patient. The averaged p-mTOR expression level in each patient was used for statistics analysis.

To measure size of individual axon spheroids in human iPSC-derived neurons in the Torin1 treatment experiment, SMI312 was used to label spheroids, while ThioflavinS was used to label amyloid plaques. Tiling images were taken in each well from a 96-well-plate and were maximum projected. Individual axonal spheroids were circled using freehand tool on ImageJ, and the circle area was measured. The total number of axonal spheroid halos analyzed ranged from 50-150 within each tilling image. Two technical replicate wells were analyzed in each experiment and three batches of experiments were performed for quantification.

To measure p-mTOR S2448 mean fluorescence intensity in individual spheroids of human neurons in the Torin1 treatment experiment, confocal images were taken for each spheroid halo (SMI312 labeled) around an amyloid plaque (ThioflavinS labeled). Individual axonal spheroids were circled using freehand tool on ImageJ, at optical sections with the maximum diameter, and mean intensity in the p-mTOR channel was measured. Similarly, axon spheroid percentage and axonal density were measured after z-stacks were maximum projected. Five spheroid halos were selected randomly in each well. Two technical replicate wells were analyzed in each experiment and three batches of experiments were done for quantification. To measure human neuron cell body size with or without Torin1 treatment, iPSC co-cultures were infected by AAV2-CB7-GFP (Addgene#105542) at titer ~7x10^9 vg/mL one week before Torin1 and amyloid beta treatment. Cells were stained with NeuN and GFP antibodies. Large field tilling imaging was performed in each well. Tilling images were maximum projected and neurons with both NeuN and GFP positive signals were measured by size, using freehand tool in ImageJ. Three technical replicate wells were analyzed in each experiment and two batches of experiments were done for quantification.

For individual axonal spheroid size measurement in the AAV9-hSyn-cre-2a-tdT infected *Mtor*-flox-5XFAD mice, anti-Lamp1 antibody was used for immunofluorescence staining to showcase the spheroid halo around amyloid plaques, ThioflavinS was used to label amyloid plaques, and anti-RFP antibody was used to reveal the tdTomato expression in infected neurons. Tilling images were taken at the somatosensory cortex of each animal. Three serial brain sections were used for tilling imaging for each mouse. An individual spheroid was counted when it was both tdTomato and Lamp1 positive. Individual spheroid size was measured using the freehand tool in ImageJ to circle the outline of spheroids, where it had the maximum diameter, followed by measurement of

the circled area. The total number of axonal spheroid halo sanalyzed ranged from 50-150 in each tilling image.

For measuring spheroid halo size in the AAV-PHPeB infected *Mtor*-flox-5XFAD experiment, anti-Lamp1 antibody was used for immunofluorescence staining to showcase the spheroid halo around amyloid plaque, ThioflavinS was used to label amyloid plaques. Tilling images were taken at the somatosensory cortex of each animal. Three serial brain sections were used for tilling imaging for each mouse. A customized ImageJ macro was used to segment individual Lamp1 positive spheroid halos and amyloid plaques (**Figure S6D**). Using a customized MATLAB program, the segmented images were processed to measure the area of individual spheroid halos and amyloid plaque area, automatically. The spheroid halo area was excluding the area in the center occupied by the amyloid plaque. The number of axonal spheroid halos and amyloid plaques analyzed ranged from 30 to 70 in each tilling image from the *Mtor*-flox-5XFAD experiment.

A customized CellProfiler program was used to automatically measure NeuN positive neuronal cell soma area of AAV-PHPeB infected *Mtor*-flox-5XFAD mice. Briefly, tilling images were taken from one hemisphere of somatosensory cortex. Tilling images were maximum projected before importing into CellProfiler (Broad Institute). The NeuN channel was set as primary object, and was used as the marker for size measurement. Three tilling images were taken from three brain sections of each animal. Three animals were used in each group.

Statistical analysis

No statistical power analysis was used to determine sample sizes, but our sample sizes were similar to those generally employed in the field. All samples were included for analysis. Excel (Microsoft), Prism (GraphPad), Qlucore Omics Explorer v3.6 (Qlucore AB, Lund, Sweden), CellProfiler v4.2.1 (Broad Institute) and RStudio (4.0.2) were used for data analysis and plotting. Statistical methods used were described in the figure legend of each relevant panel.

Data and code availability

Raw proteomics data is provided in **Table S3**. The mass spectrometry proteomics data have been deposited to the ProteomeXchange Consortium via the PRIDE partner repository with the dataset identifier PXD035197. Proteomics sample information see **Table S4**.

Lead contact

Further information and request for resources should be addressed to the correspondence authors Yifei Cai: yifei.cai@yale.edu and Jaime Grutzendler (lead contact): jaime.grutzendler@yale.edu.

Acknowledgements

This project was supported by National Institute of Health grants: RF1AG058257, R01NS115544, R01NS111961 (J.G.), a Cure Alzheimer's Fund Research Grant (J.G.), a Yale/NIDA Neuroproteomics Center Pilot Project Grant 2019 (Y.C.), a BrightFocus Foundation Postdoctoral Fellowship Program in Alzheimer's disease Research (A2021003F) (Y.C.), and a Yale ADRC grant P30 AG066508 (A.C.N). We thank Drs. Kenneth Williams, Shannon Leslie, Bobby Mathew and the Yale/NIDA Neuroproteomics Center (P30 DA018343), for providing experimental design advise, technical support and funding opportunities. We thank Dr. Anita Huttner and the Yale ADRC (P30 AG066508) for providing human postmortem AD and control brain tissues. Additional MCI and AD brain tissue was provided by the Banner Sun Health Research Institute Brain and Body Donation Program of Sun City, Arizona, supported by the NINDS (U24 NS072026), the NIA (P30 AG19610), the Arizona Department of Health Services (contract 211002), and the Arizona Biomedical Research Commission (contracts 4001, 0011, 05-901 and 1001). We thank Drs. Nur-Taz Rahman and Rolando Garcia Milian from the Yale Medical Library Bioinformatics Support Program for providing advice and technical support for bioinformatics analysis. We thank Drs. Peng Yuan, Lei Tong and Mengyang Zhang for providing MATLAB and FIJI imageJ coding for plaque and axonal spheroid quantification. We thank Dr. Philip Coish for the critical reading of this manuscript. We created schematic figures with BioRender.com

Author contributions

Y.C. and J.G. conceived and designed the study. Y.C. performed proximity labeling experiments, Y.C., R.W., M.S.M., L.T., and A.C.N. designed protein extraction, enrichment and digestion protocol, Y.C. performed protein extraction, enrichment and western blotting, J.K., R.W. and L.T. performed LC-MS-MS, protein mapping and searching, Y.C. performed proteomics data analysis and bioinformatics, A.C.N. supervised the proteomics experiments and analysis; Y.C. performed immunofluorescence and confocal imaging, D.G. performed mTOR expression characterization in MCI patients; Y.C., P.L.C. and K.J.B. refined the human iPSC-derived neuron-astrocyte co-culture protocol, P.L.C. performed lentivirus packaging, Y.C. performed AD human neuron-astrocyte co-culture, K.J.B. supervised the human neuron-astrocyte co-culture experiment; Y.C. performed AAV mediated mTOR knockout in transgenic mice, Y.C., Z.T., D.G. A.B. and K.T. performed quantifications, Y.C. performed statistics analysis; Y.C. and J.G. prepared the manuscript. J.G. supervised the study.

Declaration of interests

The authors declare no competing interests.

SUPPLEMENTARY TABLES

Table S1: Human postmortem brains information

Table S2: Full lists of new and known PAAS proteins, antibody details and immunofluorescence staining instructions

Table S3: Full lists of PAAS proteomics and neuronal soma proteomics, protein-protein interaction analysis and IPA pathway analysis

Table S4: Sample information of the proteomics dataset on Proteomexchange

REFERENCE

1. Knopman, D.S., et al., *Alzheimer disease.* Nat Rev Dis Primers, 2021. **7**(1): p. 33.
2. Spires-Jones, T.L. and B.T. Hyman, *The intersection of amyloid beta and tau at synapses in Alzheimer's disease.* Neuron, 2014. **82**(4): p. 756-71.
3. Tsai, J., et al., *Fibrillar amyloid deposition leads to local synaptic abnormalities and breakage of neuronal branches.* Nat Neurosci, 2004. **7**(11): p. 1181-3.
4. Adalbert, R., et al., *Severely dystrophic axons at amyloid plaques remain continuous and connected to viable cell bodies.* Brain, 2009. **132**(Pt 2): p. 402-16.
5. Nardocci, N. and G. Zorzi, *Axonal dystrophies.* Handb Clin Neurol, 2013. **113**: p. 1919-24.
6. Tourtellotte, W.G. and G.W. Van Hoesen, *The axonal origin of a subpopulation of dystrophic neurites in Alzheimer's disease.* Neurosci Lett, 1991. **129**(1): p. 11-6.
7. Vickers, J.C., et al., *Dystrophic neurite formation associated with age-related beta amyloid deposition in the neocortex: clues to the genesis of neurofibrillary pathology.* Exp Neurol, 1996. **141**(1): p. 1-11.
8. Yasuhara, O., et al., *Two types of dystrophic neurites in senile plaques of Alzheimer disease and elderly non-demented cases.* Neurosci Lett, 1994. **171**(1-2): p. 73-6.
9. Alzheimer, A., et al., *An English translation of Alzheimer's 1907 paper, "Uber eine eigenartige Erkankung der Hirnrinde".* Clin Anat, 1995. **8**(6): p. 429-31.
10. McKee, A.C., K.S. Kosik, and N.W. Kowall, *Neuritic pathology and dementia in Alzheimer's disease.* Ann Neurol, 1991. **30**(2): p. 156-65.
11. Kolaric, K.V., et al., *Focal axonal swellings and associated ultrastructural changes attenuate conduction velocity in central nervous system axons: a computer modeling study.* Physiol Rep, 2013. **1**(3): p. e00059.
12. Wu, Y.T., K. Gilpin, and A. Adnan, *Effects of Focal Axonal Swelling Level on the Action Potential Signal Transmission.* J Comput Neurosci, 2020. **48**(3): p. 253-263.
13. Gowrishankar, S., et al., *Massive accumulation of luminal protease-deficient axonal lysosomes at Alzheimer's disease amyloid plaques.* Proc Natl Acad Sci U S A, 2015. **112**(28): p. E3699-708.
14. Nixon, R.A., et al., *Extensive involvement of autophagy in Alzheimer disease: an immuno-electron microscopy study.* J Neuropathol Exp Neurol, 2005. **64**(2): p. 113-22.
15. Lee, S., Y. Sato, and R.A. Nixon, *Lysosomal proteolysis inhibition selectively disrupts axonal transport of degradative organelles and causes an Alzheimer's-like axonal dystrophy.* J Neurosci, 2011. **31**(21): p. 7817-30.
16. Stokin, G.B., et al., *Axonopathy and transport deficits early in the pathogenesis of Alzheimer's disease.* Science, 2005. **307**(5713): p. 1282-8.
17. Pigino, G., et al., *Disruption of fast axonal transport is a pathogenic mechanism for intraneuronal amyloid beta.* Proc Natl Acad Sci U S A, 2009. **106**(14): p. 5907-12.
18. Sadleir, K.R., et al., *Presynaptic dystrophic neurites surrounding amyloid plaques are sites of microtubule disruption, BACE1 elevation, and increased Abeta generation in Alzheimer's disease.* Acta Neuropathol, 2016. **132**(2): p. 235-56.
19. Wolfe, D.M., et al., *Autophagy failure in Alzheimer's disease and the role of defective lysosomal acidification.* European Journal of Neuroscience, 2013. **37**(12): p. 1949-1961.
20. Sanchez-Varo, R., et al., *Abnormal accumulation of autophagic vesicles correlates with axonal and synaptic pathology in young Alzheimer's mice hippocampus.* Acta Neuropathol, 2012. **123**(1): p. 53-70.
21. He, Z., et al., *Amyloid-beta plaques enhance Alzheimer's brain tau-seeded pathologies by facilitating neuritic plaque tau aggregation.* Nat Med, 2018. **24**(1): p. 29-38.

22. Knowles, R.B., et al., *Plaque-induced neurite abnormalities: implications for disruption of neural networks in Alzheimer's disease.* Proc Natl Acad Sci U S A, 1999. **96**(9): p. 5274-9.
23. Sardiello, M., et al., *A gene network regulating lysosomal biogenesis and function.* Science, 2009. **325**(5939): p. 473-7.
24. Manning, B.D. and A. Toker, *AKT/PKB Signaling: Navigating the Network.* Cell, 2017. **169**(3): p. 381-405.
25. Saxton, R.A. and D.M. Sabatini, *mTOR Signaling in Growth, Metabolism, and Disease.* Cell, 2017. **168**(6): p. 960-976.
26. C, O.N., *PI3-kinase/Akt/mTOR signaling: impaired on/off switches in aging, cognitive decline and Alzheimer's disease.* Exp Gerontol, 2013. **48**(7): p. 647-53.
27. Heras-Sandoval, D., et al., *The role of PI3K/AKT/mTOR pathway in the modulation of autophagy and the clearance of protein aggregates in neurodegeneration.* Cell Signal, 2014. **26**(12): p. 2694-701.
28. Xu, F., et al., *Roles of the PI3K/AKT/mTOR signalling pathways in neurodegenerative diseases and tumours.* Cell Biosci, 2020. **10**: p. 54.
29. Branon, T.C., et al., *Efficient proximity labeling in living cells and organisms with TurboID.* Nat Biotechnol, 2018. **36**(9): p. 880-887.
30. Rhee, H.W., et al., *Proteomic mapping of mitochondria in living cells via spatially restricted enzymatic tagging.* Science, 2013. **339**(6125): p. 1328-1331.
31. Roux, K.J., et al., *A promiscuous biotin ligase fusion protein identifies proximal and interacting proteins in mammalian cells.* J Cell Biol, 2012. **196**(6): p. 801-10.
32. Uezu, A., et al., *Identification of an elaborate complex mediating postsynaptic inhibition.* Science, 2016. **353**(6304): p. 1123-9.
33. Li, J., et al., *Cell-Surface Proteomic Profiling in the Fly Brain Uncovers Wiring Regulators.* Cell, 2020. **180**(2): p. 373-386 e15.
34. Loh, K.H., et al., *Proteomic Analysis of Unbounded Cellular Compartments: Synaptic Clefts.* Cell, 2016. **166**(5): p. 1295-1307 e21.
35. Bar, D.Z., et al., *Biotinylation by antibody recognition-a method for proximity labeling.* Nat Methods, 2018. **15**(2): p. 127-133.
36. Killinger, B.A., et al., *In situ proximity labeling identifies Lewy pathology molecular interactions in the human brain.* Proc Natl Acad Sci U S A, 2022. **119**(5).
37. Hashimoto, N., et al., *Proteomic analysis of ganglioside-associated membrane molecules: substantial basis for molecular clustering.* Proteomics, 2012. **12**(21): p. 3154-63.
38. Li, X.W., et al., *New insights into the DT40 B cell receptor cluster using a proteomic proximity labeling assay.* J Biol Chem, 2014. **289**(21): p. 14434-47.
39. Nackenoff, A.G., et al., *PLD3 is a neuronal lysosomal phospholipase D associated with beta-amyloid plaques and cognitive function in Alzheimer's disease.* PLoS Genet, 2021. **17**(4): p. e1009406.
40. Satoh, J., et al., *PLD3 is accumulated on neuritic plaques in Alzheimer's disease brains.* Alzheimers Res Ther, 2014. **6**(9): p. 70.
41. Kandalepas, P.C., et al., *The Alzheimer's beta-secretase BACE1 localizes to normal presynaptic terminals and to dystrophic presynaptic terminals surrounding amyloid plaques.* Acta Neuropathol, 2013. **126**(3): p. 329-52.
42. Yagishita, S., *Morphological investigations on axonal swellings and spheroids in various human diseases.* Virchows Arch A Pathol Anat Histol, 1978. **378**(3): p. 181-97.
43. Zhang, Y., et al., *Rapid single-step induction of functional neurons from human pluripotent stem cells.* Neuron, 2013. **78**(5): p. 785-98.

44. Bassil, R., et al., *Improved modeling of human AD with an automated culturing platform for iPSC neurons, astrocytes and microglia.* Nat Commun, 2021. **12**(1): p. 5220.
45. Thoreen, C.C., et al., *An ATP-competitive mammalian target of rapamycin inhibitor reveals rapamycin-resistant functions of mTORC1.* J Biol Chem, 2009. **284**(12): p. 8023-32.
46. Zhao, J., et al., *mTOR inhibition activates overall protein degradation by the ubiquitin proteasome system as well as by autophagy.* Proc Natl Acad Sci U S A, 2015. **112**(52): p. 15790-7.
47. Risson, V., et al., *Muscle inactivation of mTOR causes metabolic and dystrophin defects leading to severe myopathy.* J Cell Biol, 2009. **187**(6): p. 859-74.
48. Hyman, B.T., et al., *National Institute on Aging-Alzheimer's Association guidelines for the neuropathologic assessment of Alzheimer's disease.* Alzheimers Dement, 2012. **8**(1): p. 1-13.
49. Su, J.H., B.J. Cummings, and C.W. Cotman, *Identification and distribution of axonal dystrophic neurites in Alzheimer's disease.* Brain Res, 1993. **625**(2): p. 228-37.
50. Schmidt, M.L., et al., *An extensive network of PHF tau-rich dystrophic neurites permeates neocortex and nearly all neuritic and diffuse amyloid plaques in Alzheimer disease.* FEBS Lett, 1994. **344**(1): p. 69-73.
51. Drummond, E., et al., *The amyloid plaque proteome in early onset Alzheimer's disease and Down syndrome.* Acta Neuropathol Commun, 2022. **10**(1): p. 53.
52. Drummond, E., et al., *Proteomic differences in amyloid plaques in rapidly progressive and sporadic Alzheimer's disease.* Acta Neuropathol, 2017. **133**(6): p. 933-954.
53. Liao, L., et al., *Proteomic characterization of postmortem amyloid plaques isolated by laser capture microdissection.* J Biol Chem, 2004. **279**(35): p. 37061-8.
54. Torres, M., et al., *Defective lysosomal proteolysis and axonal transport are early pathogenic events that worsen with age leading to increased APP metabolism and synaptic Abeta in transgenic APP/PS1 hippocampus.* Mol Neurodegener, 2012. **7**: p. 59.
55. Vickers, J.C., et al., *Axonopathy and cytoskeletal disruption in degenerative diseases of the central nervous system.* Brain Res Bull, 2009. **80**(4-5): p. 217-23.
56. Lie, P.P.Y., et al., *Axonal transport of late endosomes and amphisomes is selectively modulated by local Ca(2+) efflux and disrupted by PSEN1 loss of function.* Sci Adv, 2022. **8**(17): p. eabj5716.
57. Blanchard, J.W., et al., *Reconstruction of the human blood-brain barrier in vitro reveals a pathogenic mechanism of APOE4 in pericytes.* Nat Med, 2020. **26**(6): p. 952-963.
58. Espuny-Camacho, I., et al., *Hallmarks of Alzheimer's Disease in Stem-Cell-Derived Human Neurons Transplanted into Mouse Brain.* Neuron, 2017. **93**(5): p. 1066-1081 e8.
59. Israel, M.A., et al., *Probing sporadic and familial Alzheimer's disease using induced pluripotent stem cells.* Nature, 2012. **482**(7384): p. 216-20.
60. Wang, M., et al., *Transformative Network Modeling of Multi-omics Data Reveals Detailed Circuits, Key Regulators, and Potential Therapeutics for Alzheimer's Disease.* Neuron, 2021. **109**(2): p. 257-272 e14.
61. Tracy, T.E., et al., *Tau interactome maps synaptic and mitochondrial processes associated with neurodegeneration.* Cell, 2022. **185**(4): p. 712-728 e14.
62. Meyer-Luehmann, M., et al., *Rapid appearance and local toxicity of amyloid-beta plaques in a mouse model of Alzheimer's disease.* Nature, 2008. **451**(7179): p. 720-4.
63. Yuan, P., et al., *TREM2 Haplodeficiency in Mice and Humans Impairs the Microglia Barrier Function Leading to Decreased Amyloid Compaction and Severe Axonal Dystrophy.* Neuron, 2016. **92**(1): p. 252-264.
64. Roney, J.C., et al., *Lipid-mediated motor-adaptor sequestration impairs axonal lysosome delivery leading to autophagic stress and dystrophy in Niemann-Pick type C.* Dev Cell, 2021. **56**(10): p. 1452-1468 e8.

65. Satoh, J.I., et al., *Alzheimer's disease pathology in Nasu-Hakola disease brains.* Intractable Rare Dis Res, 2018. **7**(1): p. 32-36.
66. Foulds, N., et al., *Adult-Onset Leukoencephalopathy with Axonal Spheroids and Pigmented Glia Caused by a Novel R782G Mutation in CSF1R.* Sci Rep, 2015. **5**: p. 10042.
67. DiFiglia, M., et al., *Aggregation of huntingtin in neuronal intranuclear inclusions and dystrophic neurites in brain.* Science, 1997. **277**(5334): p. 1990-3.
68. Gonzalez, A.C., et al., *Unconventional Trafficking of Mammalian Phospholipase D3 to Lysosomes.* Cell Rep, 2018. **22**(4): p. 1040-1053.
69. Cruchaga, C., et al., *Rare coding variants in the phospholipase D3 gene confer risk for Alzheimer's disease.* Nature, 2014. **505**(7484): p. 550-554.
70. Goltsev, Y., et al., *Deep Profiling of Mouse Splenic Architecture with CODEX Multiplexed Imaging.* Cell, 2018. **174**(4): p. 968-981 e15.
71. Sharoar, M.G., et al., *Sequential formation of different layers of dystrophic neurites in Alzheimer's brains.* Mol Psychiatry, 2019. **24**(9): p. 1369-1382.
72. Masliah, E., et al., *An antibody against phosphorylated neurofilaments identifies a subset of damaged association axons in Alzheimer's disease.* Am J Pathol, 1993. **142**(3): p. 871-82.
73. Dickson, T.C., et al., *Neurochemical diversity of dystrophic neurites in the early and late stages of Alzheimer's disease.* Exp Neurol, 1999. **156**(1): p. 100-10.
74. Hoffman, G.E., et al., *Transcriptional signatures of schizophrenia in hiPSC-derived NPCs and neurons are concordant with post-mortem adult brains.* Nat Commun, 2017. **8**(1): p. 2225.
75. Oakley, H., et al., *Intraneuronal beta-amyloid aggregates, neurodegeneration, and neuron loss in transgenic mice with five familial Alzheimer's disease mutations: potential factors in amyloid plaque formation.* J Neurosci, 2006. **26**(40): p. 10129-40.
76. Sun, Y., et al., *C9orf72 arginine-rich dipeptide repeats inhibit UPF1-mediated RNA decay via translational repression.* Nat Commun, 2020. **11**(1): p. 3354.
77. Zhang, Y., et al., *Purification and Characterization of Progenitor and Mature Human Astrocytes Reveals Transcriptional and Functional Differences with Mouse.* Neuron, 2016. **89**(1): p. 37-53.
78. Uhlen, M., et al., *Proteomics. Tissue-based map of the human proteome.* Science, 2015. **347**(6220): p. 1260419.
79. Chen, J., et al., *ToppGene Suite for gene list enrichment analysis and candidate gene prioritization.* Nucleic Acids Res, 2009. **37**(Web Server issue): p. W305-11.
80. Szklarczyk, D., et al., *STRING v11: protein-protein association networks with increased coverage, supporting functional discovery in genome-wide experimental datasets.* Nucleic Acids Res, 2019. **47**(D1): p. D607-D613.
81. Shannon, P., et al., *Cytoscape: a software environment for integrated models of biomolecular interaction networks.* Genome Res, 2003. **13**(11): p. 2498-504.
82. Bader, G.D. and C.W. Hogue, *An automated method for finding molecular complexes in large protein interaction networks.* BMC Bioinformatics, 2003. **4**: p. 2.
83. Wang, J., et al., *WebGestalt 2017: a more comprehensive, powerful, flexible and interactive gene set enrichment analysis toolkit.* Nucleic Acids Res, 2017. **45**(W1): p. W130-W137.
84. Kramer, A., et al., *Causal analysis approaches in Ingenuity Pathway Analysis.* Bioinformatics, 2014. **30**(4): p. 523-30.
85. Subramanian, A., et al., *Gene set enrichment analysis: a knowledge-based approach for interpreting genome-wide expression profiles.* Proc Natl Acad Sci U S A, 2005. **102**(43): p. 15545-50.
86. Li, A., et al., *Using the dCas9-KRAB system to repress gene expression in hiPSC-derived NGN2 neurons.* STAR Protoc, 2021. **2**(2): p. 100580.

87. Ho, S.M., et al., *Rapid Ngn2-induction of excitatory neurons from hiPSC-derived neural progenitor cells.* Methods, 2016. **101**: p. 113-24.
88. Murakami, M., et al., *mTOR is essential for growth and proliferation in early mouse embryos and embryonic stem cells.* Mol Cell Biol, 2004. **24**(15): p. 6710-8.

Figure 1

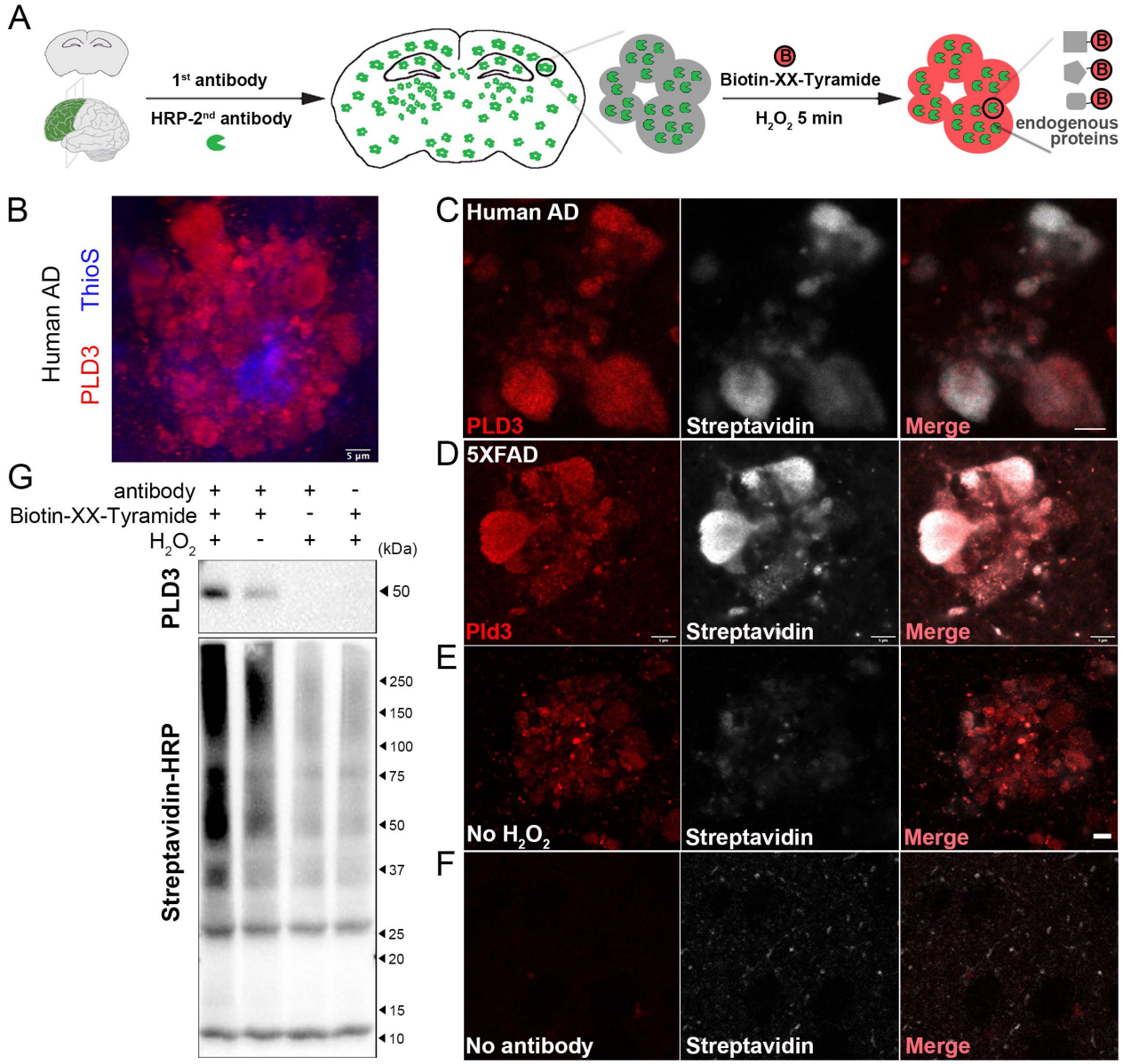
A
1st antibody
HRP-2nd antibody
Biotin-XX-Tyramide
H2O2 5 min
endogenous proteins
B
Human AD
ThioS
PLD3
5 µm
C
Human AD
PLD3
Streptavidin
Merge
D
5XFAD
Pld3
Streptavidin
Merge
E
No H2O2
Streptavidin
Merge
F
No antibody
Streptavidin
Merge
G
antibody + + + -
Biotin-XX-Tyramide + + - +
H2O2 + - + +
(kDa)
PLD3
50
Streptavidin-HRP
250
150
100
75
50
37
25
20
15
10

Figure 2

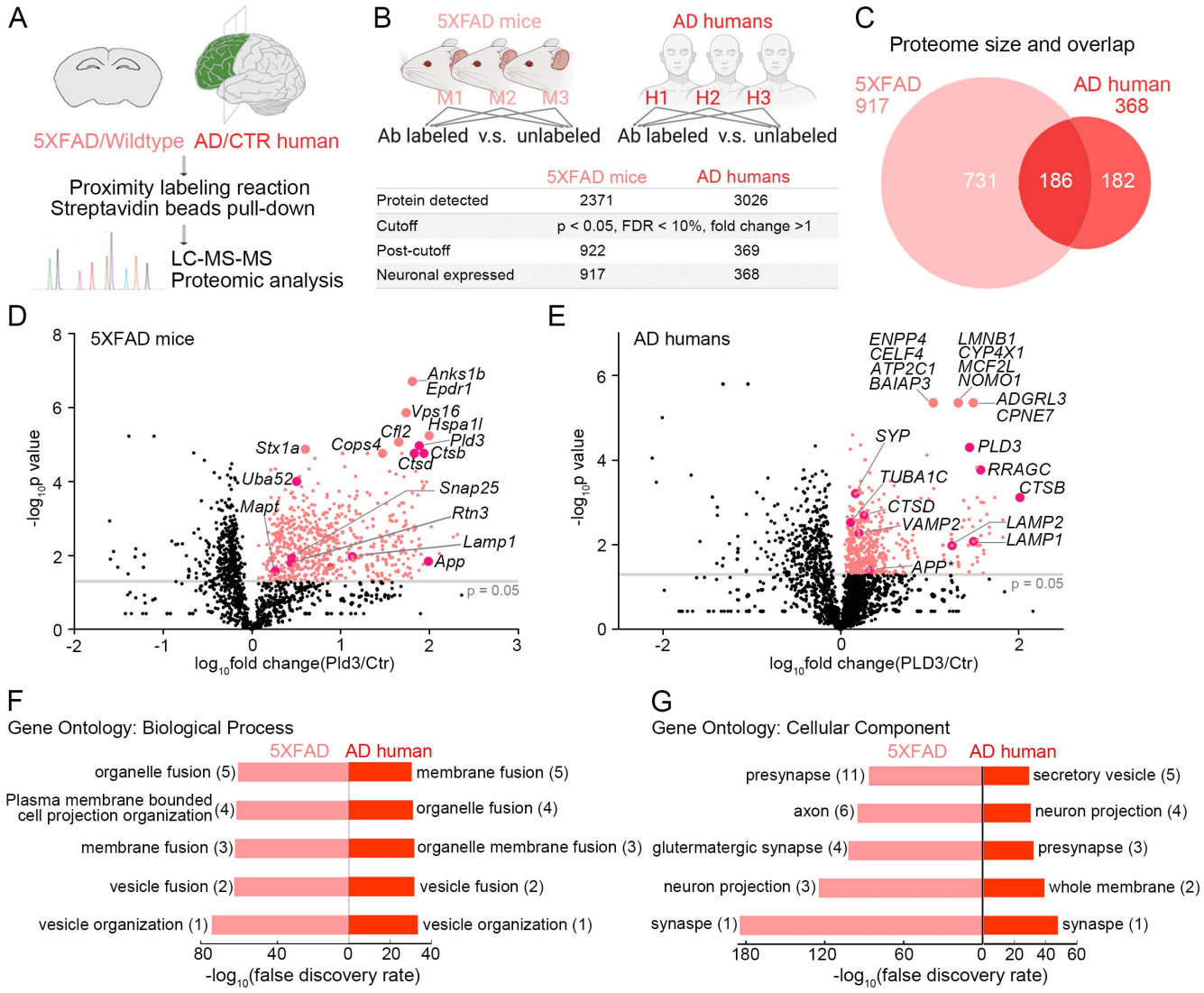

	5XFAD mice	AD humans
Protein detected	2371	3026
Cutoff	$p < 0.05$, FDR < 10%, fold change >1	
Post-cutoff	922	369
Neuronal expressed	917	368

Figure 3

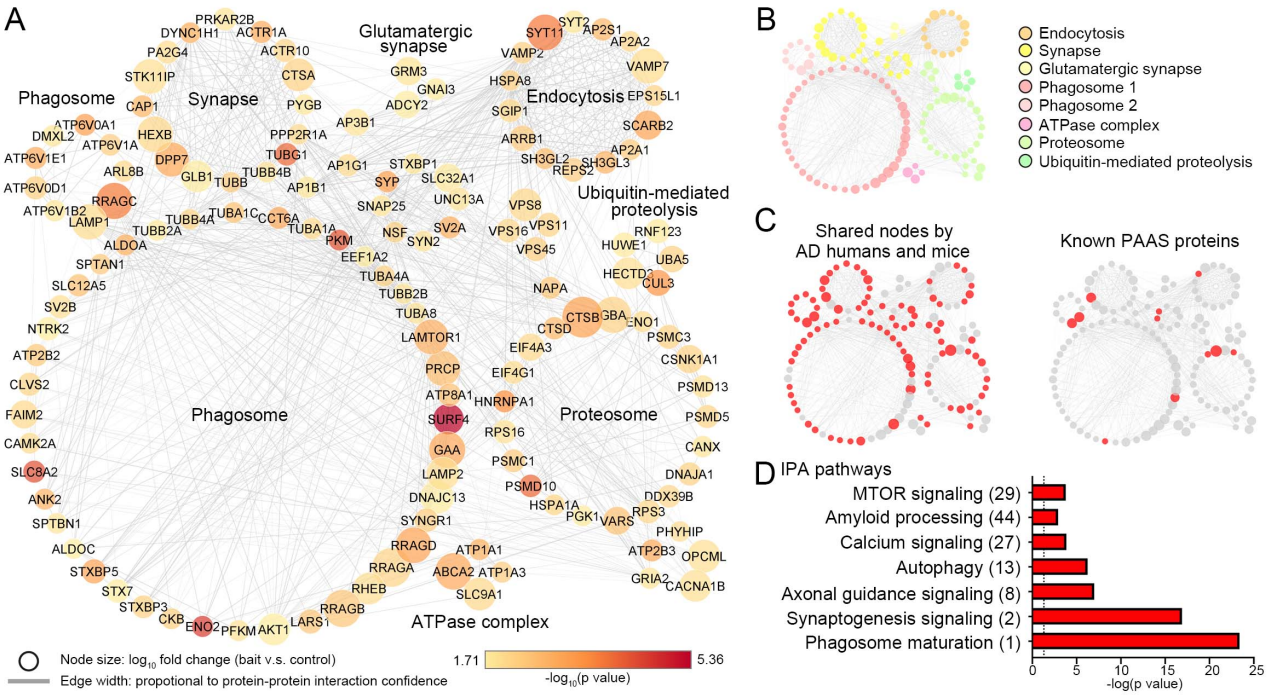
A
Glutamatergic synapse
Phagosome
Synapse
Endocytosis
Ubiquitin-mediated proteolysis
Phagosome
Proteosome
ATPase complex
Node size: log_{10} fold change (bait v.s. control)
Edge width: propotional to protein-protein interaction confidence
1.71
5.36
$-log_{10}$(p value)
B
Endocytosis
Synapse
Glutamatergic synapse
Phagosome 1
Phagosome 2
ATPase complex
Proteosome
Ubiquitin-mediated proteolysis
C
Shared nodes by AD humans and mice
Known PAAS proteins
D
IPA pathways
MTOR signaling (29)
Amyloid processing (44)
Calcium signaling (27)
Autophagy (13)
Axonal guidance signaling (8)
Synaptogenesis signaling (2)
Phagosome maturation (1)
0
5
10
15
20
25
-log(p value)

E

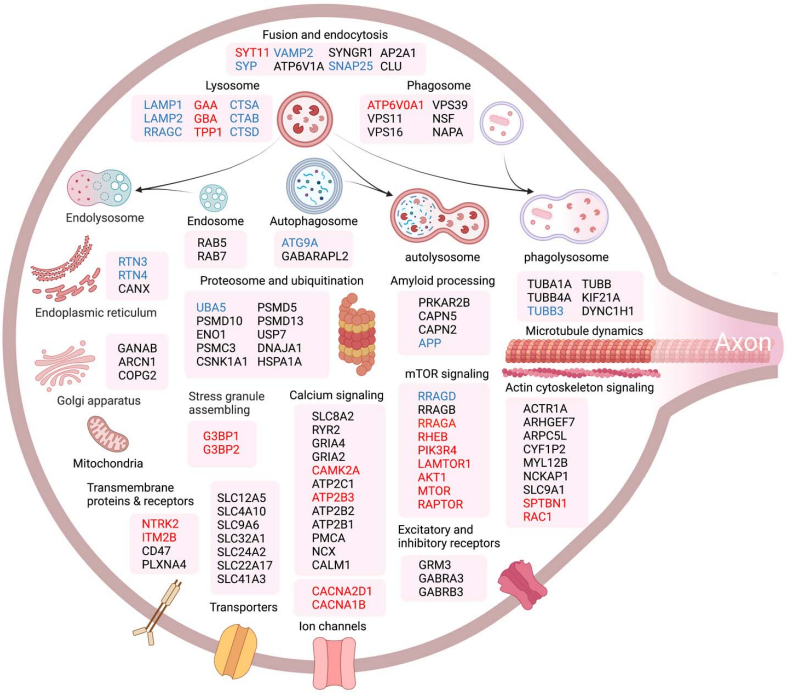
Fusion and endocytosis
SYT11 VAMP2 SYNGR1 AP2A1
SYP ATP6V1A SNAP25 CLU
Lysosome
LAMP1 GAA CTSA
LAMP2 GBA CTAB
RRAGC TPP1 CTSD
Phagosome
ATP6V0A1 VPS39
VPS11 NSF
VPS16 NAPA
Endolysosome
Endosome
Autophagosome
autolysosome
phagolysosome
RAB5
RAB7
ATG9A
GABARAPL2
Endoplasmic reticulum
RTN3
RTN4
CANX
Proteosome and ubiquitination
UBA5 PSMD5
PSMD10 PSMD13
ENO1 USP7
PSMC3 DNAJA1
CSNK1A1 HSPA1A
Amyloid processing
PRKAR2B
CAPN5
CAPN2
APP
TUBA1A TUBB
TUBB4A KIF21A
TUBB3 DYNC1H1
Microtubule dynamics
Axon
Golgi apparatus
GANAB
ARCN1
COPG2
Stress granule assembling
G3BP1
G3BP2
Calcium signaling
SLC8A2
RYR2
GRIA4
GRIA2
CAMK2A
ATP2C1
ATP2B3
ATP2B2
ATP2B1
PMCA
NCX
CALM1
mTOR signaling
RRAGD
RRAGB
RRAGA
RHEB
PIK3R4
LAMTOR1
AKT1
MTOR
RAPTOR
Actin cytoskeleton signaling
ACTR1A
ARHGEF7
ARPC5L
CYF1P2
MYL12B
NCKAP1
SLC9A1
SPTBN1
RAC1
Mitochondria
Transmembrane proteins & receptors
NTRK2
ITM2B
CD47
PLXNA4
SLC12A5
SLC4A10
SLC9A6
SLC32A1
SLC24A2
SLC22A17
SLC41A3
Transporters
CACNA2D1
CACNA1B
Ion channels
Excitatory and inhibitory receptors
GRM3
GABRA3
GABRB3

Figure 4

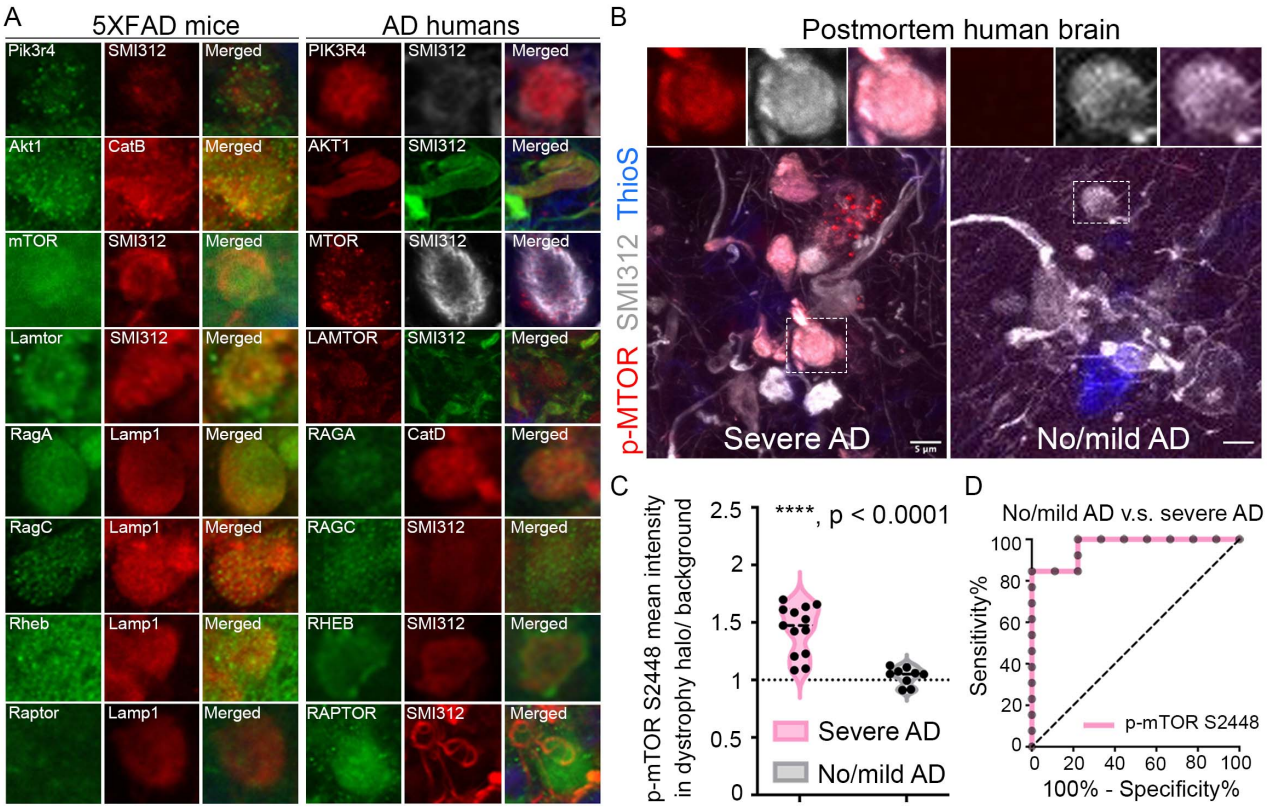
A
5XFAD mice
AD humans
Pik3r4
SMI312
Merged
PIK3R4
Akt1
CatB
AKT1
mTOR
MTOR
Lamtor
LAMTOR
RagA
Lamp1
RAGA
CatD
RagC
RAGC
Rheb
RHEB
Raptor
RAPTOR
B
Postmortem human brain
p-MTOR SMI312 ThioS
Severe AD
No/mild AD
C
p-mTOR S2448 mean intensity in dystrophy halo/ background
****, p < 0.0001
Severe AD
No/mild AD
D
No/mild AD v.s. severe AD
Sensitivity%
100% - Specificity%
p-mTOR S2448

Figure 5

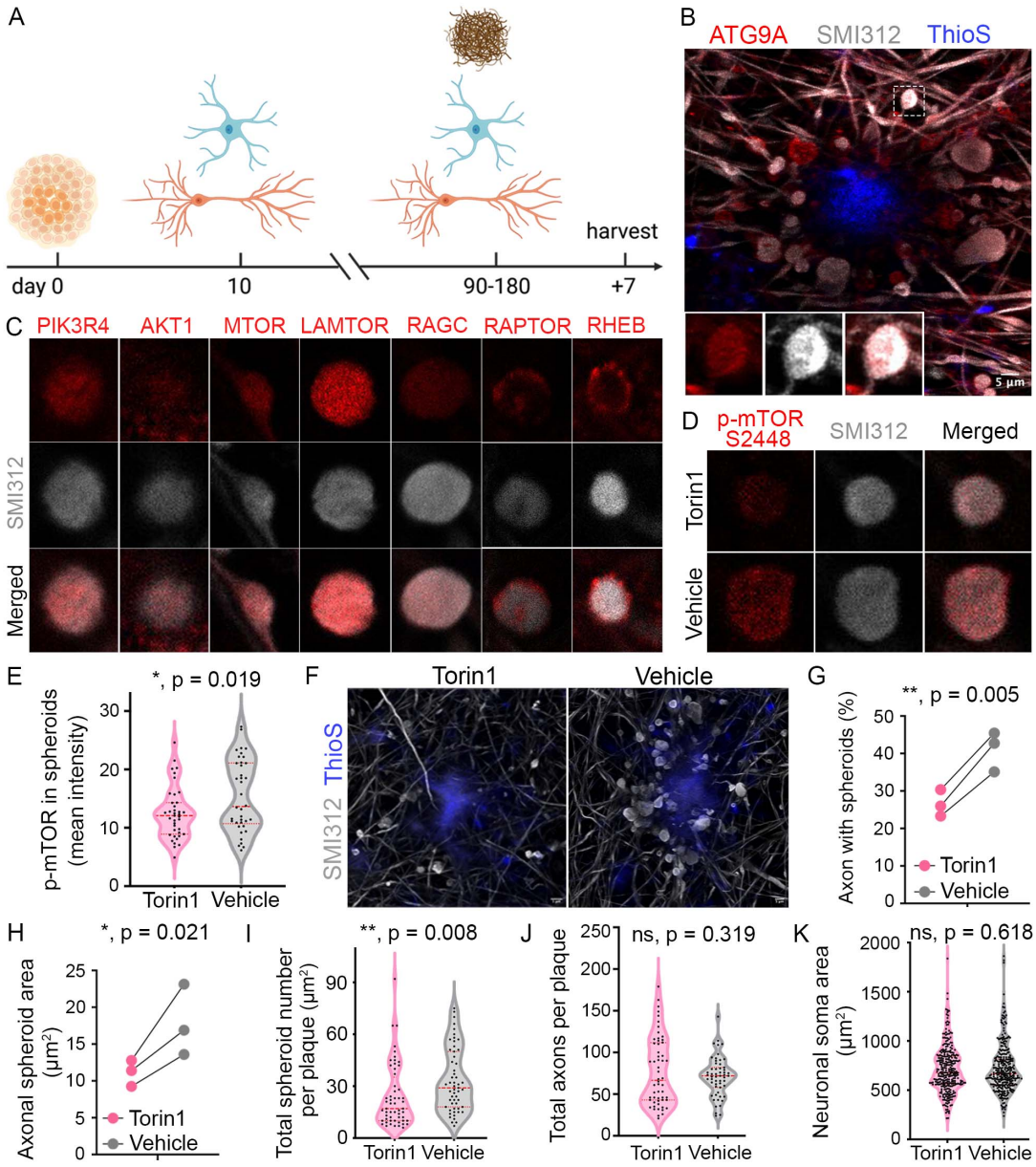
A
day 0
10
90-180
+7
harvest
B
ATG9A
SMI312
ThioS
5 µm
C
PIK3R4
AKT1
MTOR
LAMTOR
RAGC
RAPTOR
RHEB
SMI312
Merged
D
p-mTOR S2448
SMI312
Merged
Torin1
Vehicle
E
*, p = 0.019
p-mTOR in spheroids (mean intensity)
Torin1
Vehicle
F
Torin1
Vehicle
SMI312 ThioS
G
**, p = 0.005
Axon with spheroids (%)
Torin1
Vehicle
H
*, p = 0.021
Axonal spheroid area (µm²)
Torin1
Vehicle
I
**, p = 0.008
Total spheroid number per plaque (µm²)
Torin1
Vehicle
J
ns, p = 0.319
Total axons per plaque
Torin1
Vehicle
K
ns, p = 0.618
Neuronal soma area (µm²)
Torin1
Vehicle

Figure 6

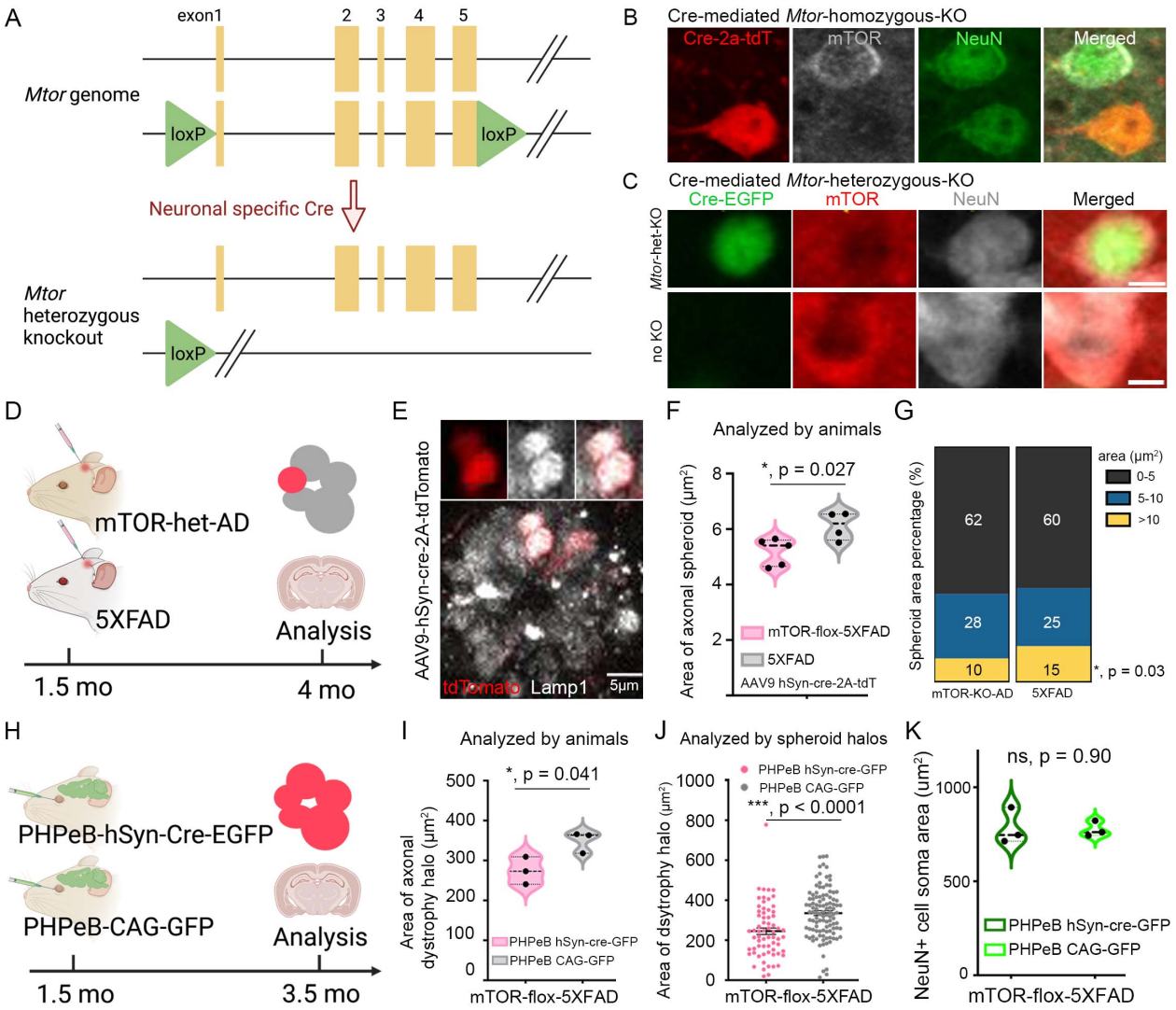
A
exon1
2
3
4
5
Mtor genome
loxP
loxP
Neuronal specific Cre
Mtor heterozygous knockout
loxP
B
Cre-mediated Mtor-homozygous-KO
Cre-2a-tdT
mTOR
NeuN
Merged
C
Cre-mediated Mtor-heterozygous-KO
Cre-EGFP
mTOR
NeuN
Merged
Mtor-het-KO
no KO
D
mTOR-het-AD
5XFAD
Analysis
1.5 mo
4 mo
E
AAV9-hSyn-cre-2A-tdTomato
tdTomato
Lamp1
5μm
F
Analyzed by animals
*, p = 0.027
Area of axonal spheroid (μm²)
mTOR-flox-5XFAD
5XFAD
AAV9 hSyn-cre-2A-tdT
G
area (μm²)
0-5
5-10
>10
Spheroid area percentage (%)
62
60
28
25
10
15
*, p = 0.03
mTOR-KO-AD
5XFAD
H
PHPeB-hSyn-Cre-EGFP
PHPeB-CAG-GFP
Analysis
1.5 mo
3.5 mo
I
Analyzed by animals
*, p = 0.041
Area of axonal dystrophy halo (μm²)
PHPeB hSyn-cre-GFP
PHPeB CAG-GFP
mTOR-flox-5XFAD
J
Analyzed by spheroid halos
PHPeB hSyn-cre-GFP
PHPeB CAG-GFP
***, p < 0.0001
Area of dystrophy halo (μm²)
mTOR-flox-5XFAD
K
ns, p = 0.90
NeuN+ cell soma area (μm²)
PHPeB hSyn-cre-GFP
PHPeB CAG-GFP
mTOR-flox-5XFAD

Figure S1

A

	# of donors	age (years)	gender (f:m)	PMI (h)	ABC score
AD	3	77±12	2:1	13.5±6.5	A2-3, B3, C2-3
CTR	3	84±1	1:2	19±8	A0-1, B1, C0

B

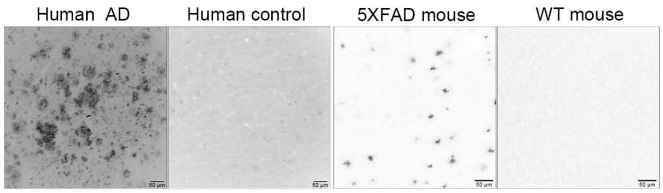

C

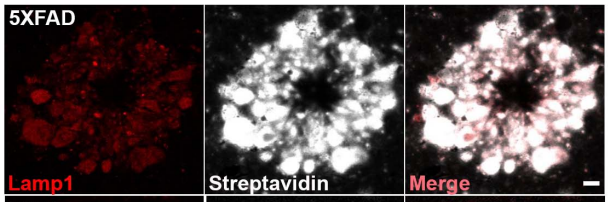

D

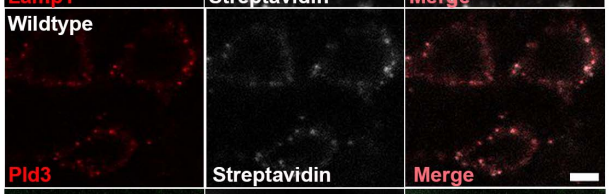

E

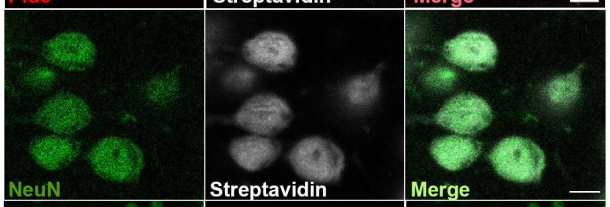

F

G

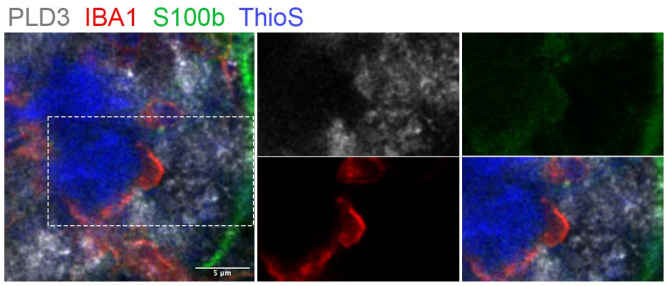

H

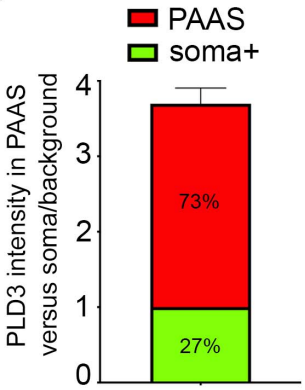

I

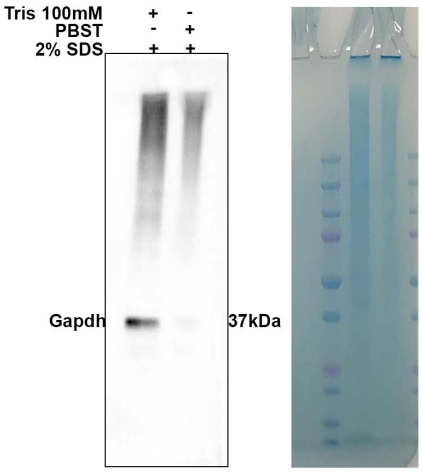

H

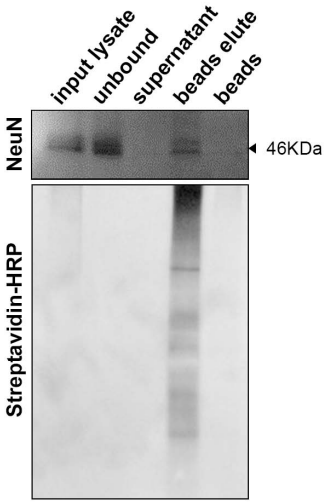

I

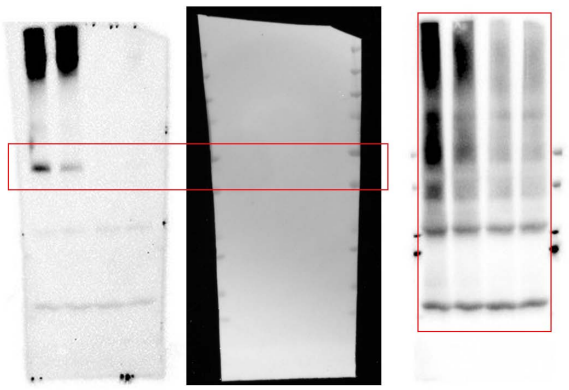

PLD3 blot Bright field Streptavidin-HRP blot

J

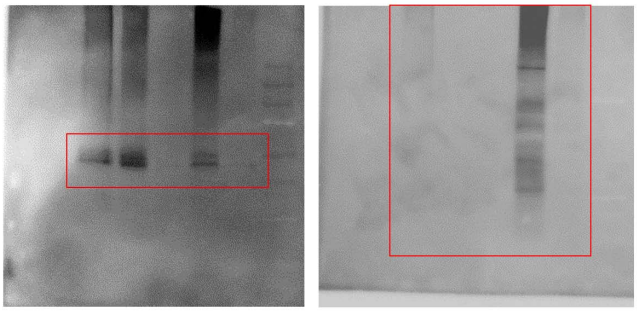

NeuN blot Streptavidin-HRP blot

Figure S2

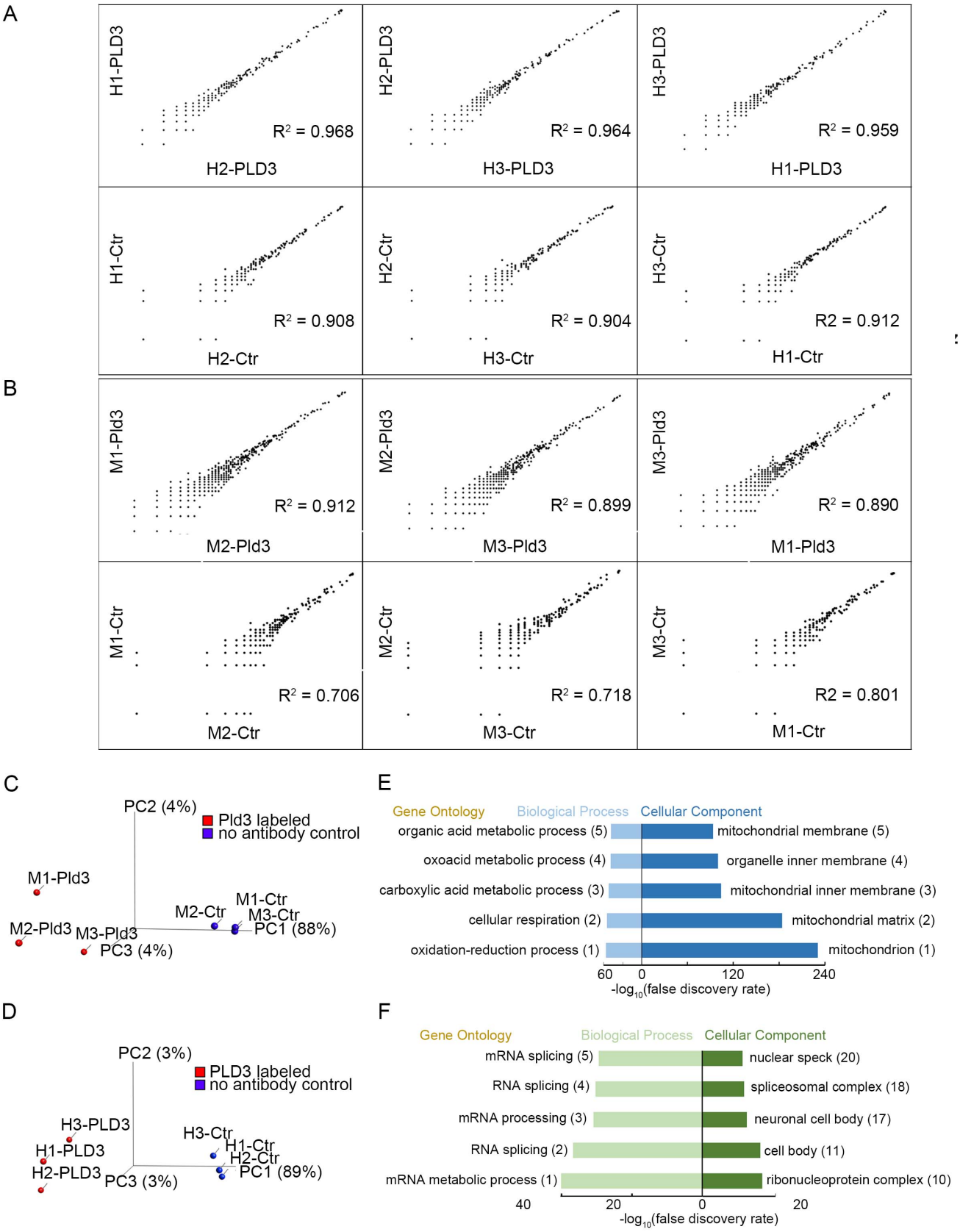
A
H1-PLD3
H2-PLD3
R² = 0.968
H2-PLD3
H3-PLD3
R² = 0.964
H3-PLD3
H1-PLD3
R² = 0.959
H1-Ctr
H2-Ctr
R² = 0.908
H2-Ctr
H3-Ctr
R² = 0.904
H3-Ctr
H1-Ctr
R2 = 0.912
B
M1-Pld3
M2-Pld3
R² = 0.912
M2-Pld3
M3-Pld3
R² = 0.899
M3-Pld3
M1-Pld3
R² = 0.890
M1-Ctr
M2-Ctr
R² = 0.706
M2-Ctr
M3-Ctr
R² = 0.718
M3-Ctr
M1-Ctr
R2 = 0.801
C
PC2 (4%)
Pld3 labeled
no antibody control
M1-Pld3
M1-Ctr
M2-Ctr
M3-Ctr
PC1 (88%)
M2-Pld3
M3-Pld3
PC3 (4%)
D
PC2 (3%)
PLD3 labeled
no antibody control
H3-PLD3
H3-Ctr
H1-PLD3
H1-Ctr
H2-Ctr
H2-PLD3
PC3 (3%)
PC1 (89%)
E
Gene Ontology
Biological Process
Cellular Component
organic acid metabolic process (5)
mitochondrial membrane (5)
oxoacid metabolic process (4)
organelle inner membrane (4)
carboxylic acid metabolic process (3)
mitochondrial inner membrane (3)
cellular respiration (2)
mitochondrial matrix (2)
oxidation-reduction process (1)
mitochondrion (1)
60
0
120
240
-log10(false discovery rate)
F
Gene Ontology
Biological Process
Cellular Component
mRNA splicing (5)
nuclear speck (20)
RNA splicing (4)
spliceosomal complex (18)
mRNA processing (3)
neuronal cell body (17)
RNA splicing (2)
cell body (11)
mRNA metabolic process (1)
ribonucleoprotein complex (10)
40
20
0
20
-log10(false discovery rate)

Figure S3-1

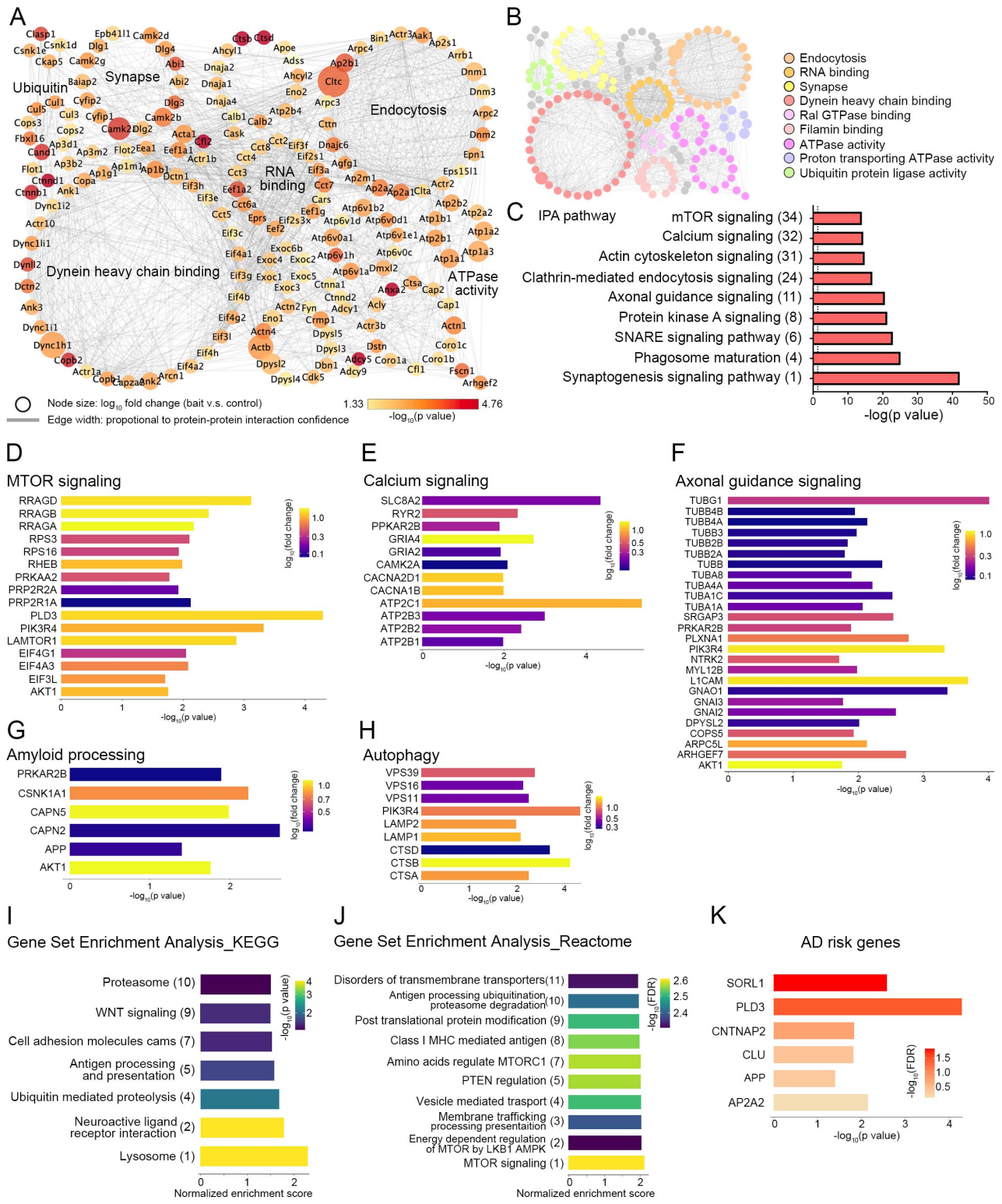
A
Synapse
Ubiquitin
Endocytosis
RNA binding
Dynein heavy chain binding
ATPase activity
Node size: log10 fold change (bait v.s. control)
Edge width: propotional to protein-protein interaction confidence
1.33
4.76
-log10(p value)
B
Endocytosis
RNA binding
Synapse
Dynein heavy chain binding
Ral GTPase binding
Filamin binding
ATPase activity
Proton transporting ATPase activity
Ubiquitin protein ligase activity
C
IPA pathway
mTOR signaling (34)
Calcium signaling (32)
Actin cytoskeleton signaling (31)
Clathrin-mediated endocytosis signaling (24)
Axonal guidance signaling (11)
Protein kinase A signaling (8)
SNARE signaling pathway (6)
Phagosome maturation (4)
Synaptogenesis signaling pathway (1)
-log(p value)
D
MTOR signaling
RRAGD
RRAGB
RRAGA
RPS3
RPS16
RHEB
PRKAA2
PRP2R2A
PRP2R1A
PLD3
PIK3R4
LAMTOR1
EIF4G1
EIF4A3
EIF3L
AKT1
-log10(p value)
log10(fold change)
E
Calcium signaling
SLC8A2
RYR2
PPKAR2B
GRIA4
GRIA2
CAMK2A
CACNA2D1
CACNA1B
ATP2C1
ATP2B3
ATP2B2
ATP2B1
-log10(p value)
log10(fold change)
F
Axonal guidance signaling
TUBG1
TUBB4B
TUBB4A
TUBB3
TUBB2B
TUBB2A
TUBB
TUBA8
TUBA4A
TUBA1C
TUBA1A
SRGAP3
PRKAR2B
PLXNA1
PIK3R4
NTRK2
MYL12B
L1CAM
GNAO1
GNAI3
GNAI2
DPYSL2
COPS5
ARPC5L
ARHGEF7
AKT1
-log10(p value)
log10(fold change)
G
Amyloid processing
PRKAR2B
CSNK1A1
CAPN5
CAPN2
APP
AKT1
-log10(p value)
log10(fold change)
H
Autophagy
VPS39
VPS16
VPS11
PIK3R4
LAMP2
LAMP1
CTSD
CTSB
CTSA
-log10(p value)
log10(fold change)
I
Gene Set Enrichment Analysis_KEGG
Proteasome (10)
WNT signaling (9)
Cell adhesion molecules cams (7)
Antigen processing and presentation (5)
Ubiquitin mediated proteolysis (4)
Neuroactive ligand receptor interaction (2)
Lysosome (1)
Normalized enrichment score
-log10(p value)
J
Gene Set Enrichment Analysis_Reactome
Disorders of transmembrane transporters(11)
Antigen processing ubiquitination proteasome degradation (10)
Post translational protein modification (9)
Class I MHC mediated antigen (8)
Amino acids regulate MTORC1 (7)
PTEN regulation (5)
Vesicle mediated trasport (4)
Membrane trafficking processing presentation (3)
Energy dependent regulation of MTOR by LKB1 AMPK (2)
MTOR signaling (1)
Normalized enrichment score
-log10(FDR)
K
AD risk genes
SORL1
PLD3
CNTNAP2
CLU
APP
AP2A2
-log10(p value)
-log10(FDR)

Figure S3-2

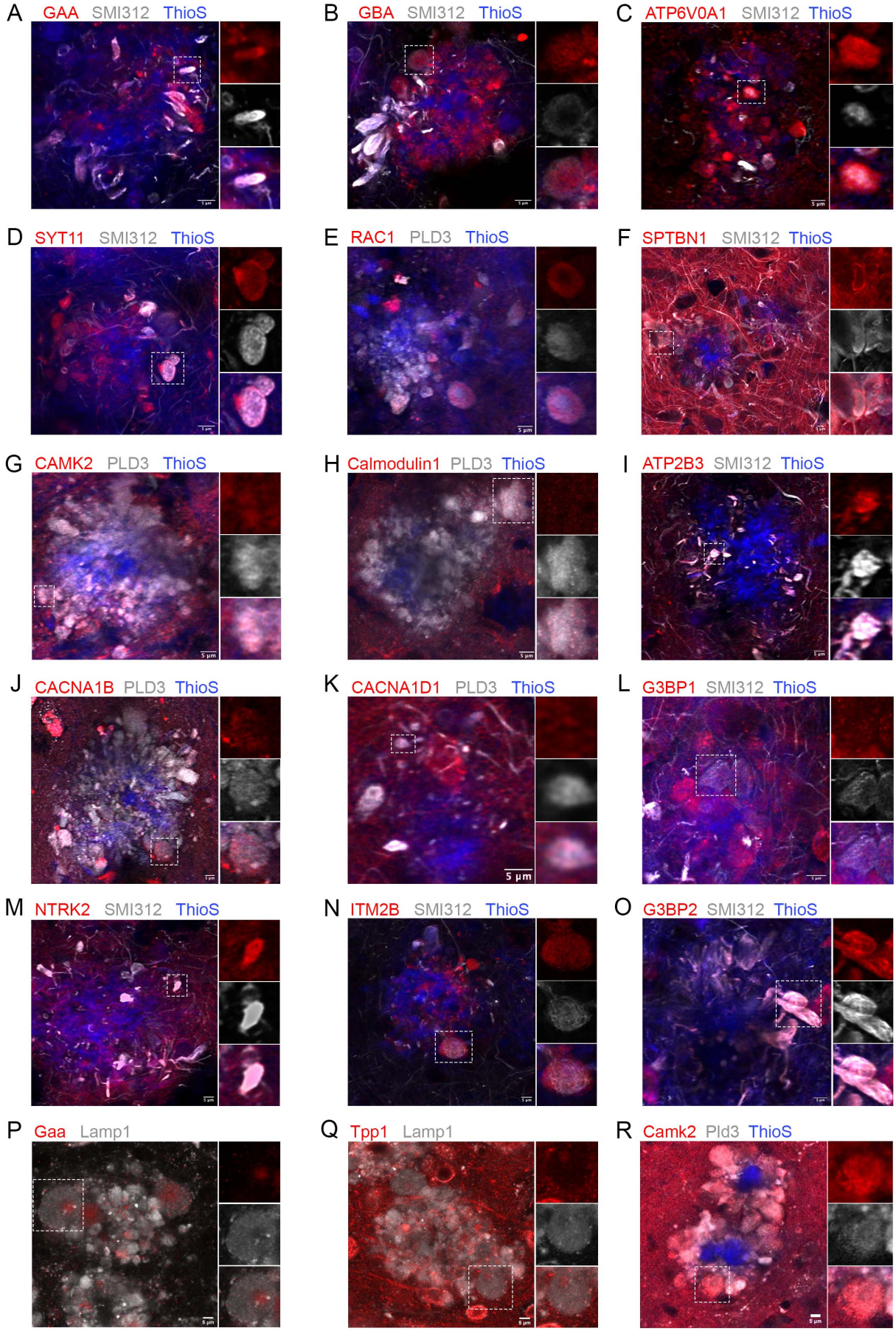
A GAA SMI312 ThioS
B GBA SMI312 ThioS
C ATP6V0A1 SMI312 ThioS
D SYT11 SMI312 ThioS
E RAC1 PLD3 ThioS
F SPTBN1 SMI312 ThioS
G CAMK2 PLD3 ThioS
H Calmodulin1 PLD3 ThioS
I ATP2B3 SMI312 ThioS
J CACNA1B PLD3 ThioS
K CACNA1D1 PLD3 ThioS
5 µm
L G3BP1 SMI312 ThioS
M NTRK2 SMI312 ThioS
N ITM2B SMI312 ThioS
O G3BP2 SMI312 ThioS
P Gaa Lamp1
Q Tpp1 Lamp1
R Camk2 Pld3 ThioS

Figure S4

A

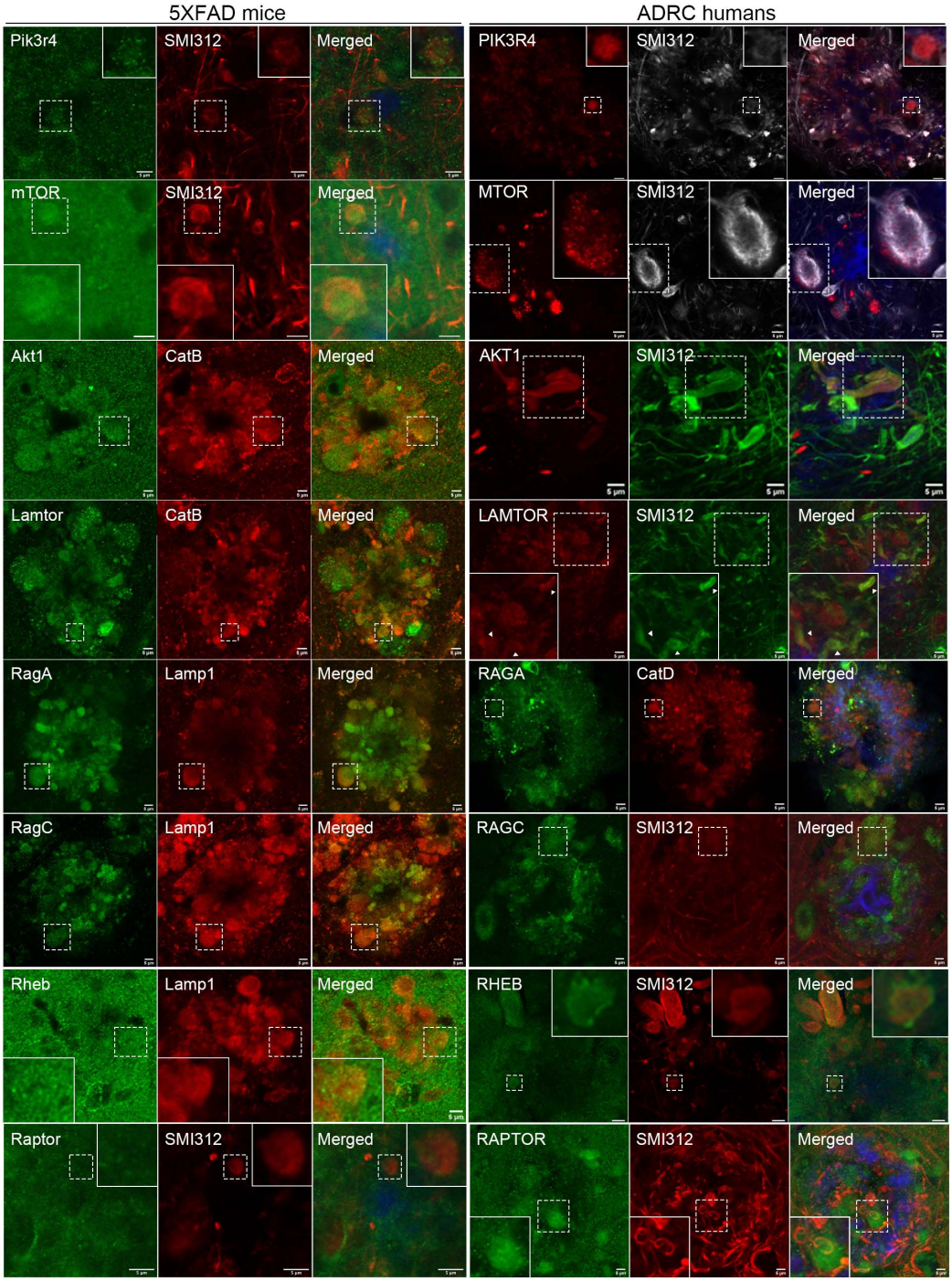

S4B

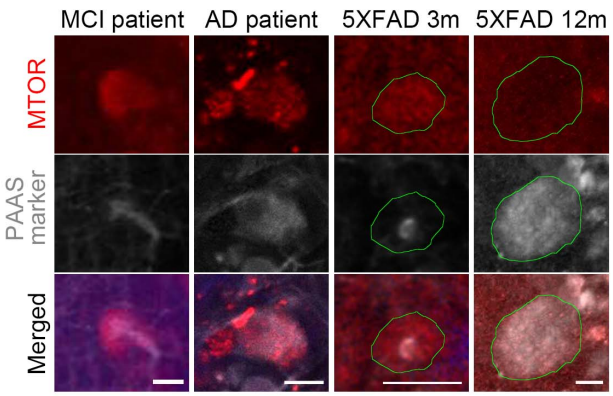

Figure S5

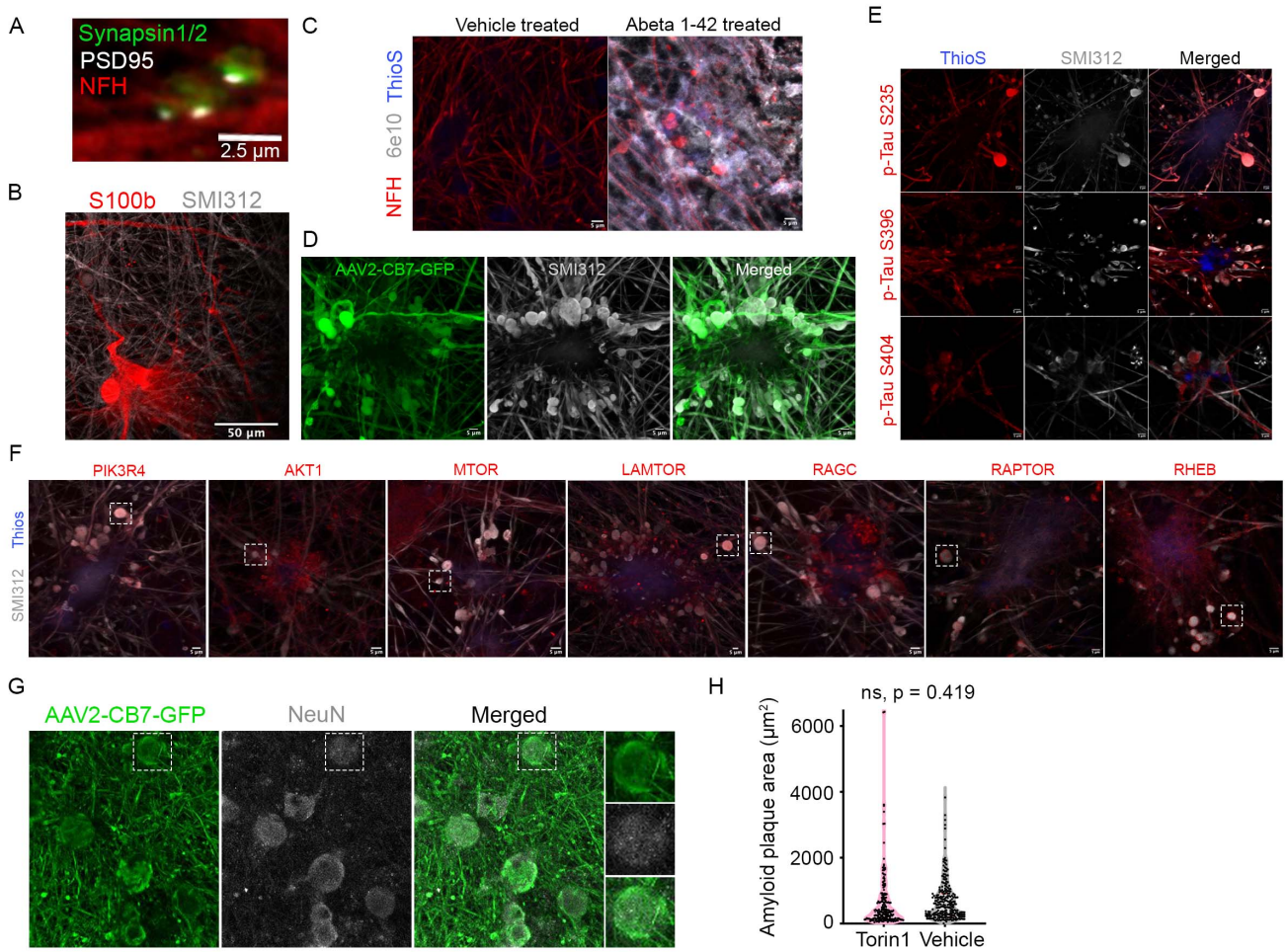
A
Synapsin1/2
PSD95
NFH
2.5 µm
B
S100b
SMI312
50 µm
C
Vehicle treated
Abeta 1-42 treated
ThioS
6e10
NFH
D
AAV2-CB7-GFP
SMI312
Merged
E
ThioS
SMI312
Merged
p-Tau S235
p-Tau S396
p-Tau S404
F
PIK3R4
AKT1
MTOR
LAMTOR
RAGC
RAPTOR
RHEB
Thios
SMI312

G
AAV2-CB7-GFP
NeuN
Merged

H
ns, p = 0.419
Amyloid plaque area (µm²)
6000
4000
2000
0
Torin1
Vehicle

Figure S6

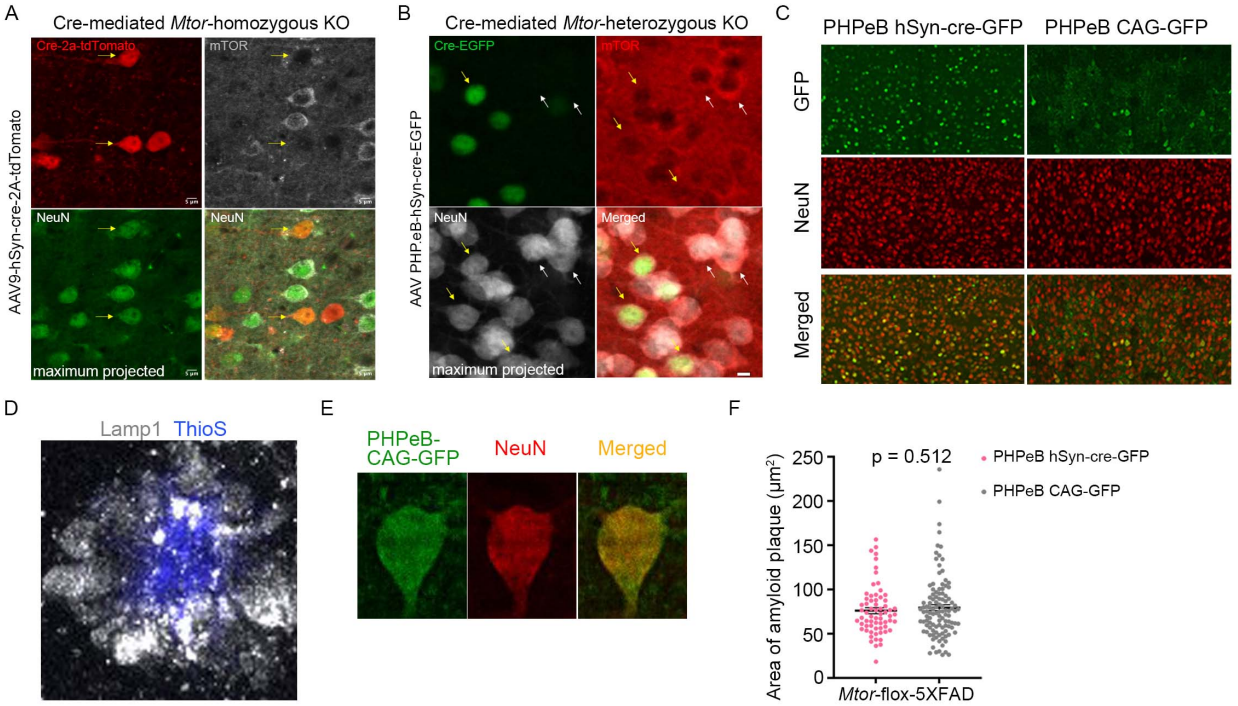
A
Cre-mediated *Mtor*-homozygous KO
AAV9-hSyn-cre-2A-tdTomato
Cre-2a-tdTomato
mTOR
NeuN
NeuN
maximum projected
B
Cre-mediated *Mtor*-heterozygous KO
AAV PHP.eB-hSyn-cre-EGFP
Cre-EGFP
mTOR
NeuN
Merged
maximum projected
C
PHPeB hSyn-cre-GFP
PHPeB CAG-GFP
GFP
NeuN
Merged
D
Lamp1 ThioS
E
PHPeB-CAG-GFP
NeuN
Merged
F
p = 0.512
PHPeB hSyn-cre-GFP
PHPeB CAG-GFP
Area of amyloid plaque (μm²)
250
200
150
100
50
0
Mtor-flox-5XFAD